Mineralogical and geochemical insights of Fe-Ti-P-REE mineralization in alkaline igneous complexes: example from the Kodal deposit, Oslo Rift, Norway

Pierre Buelens[1], Vinciane Debaille[1], Sophie Decrée[2], Nolwenn Coint[3]
[1]*Laboratoire G-Time, Université Libre de Bruxelles, Brussels, Belgium*
[2]*Royal Belgian Institute of Natural Sciences, Geological Survey of Belgium, Brussels, Belgium*
[3]*Geological Survey of Norway, Trondheim, Norway*

Abstract. Phosphates are essential in our society to guarantee the global food production chain. They have been recognized as critical raw materials (CRM) by the EU. It is mostly extracted from apatite $[Ca_5(PO_4)_3(F, OH, Cl)]$, a mineral common to sedimentary, igneous and metamorphic rocks. Alkaline igneous deposits have so far received limited interest by comparison with other igneous or sedimentary-related type deposits. However, some of them show notable enrichments in P_2O_5 and could become exploitable, especially in Europe. In these systems, apatite is enriched in Rare Earth Elements (REE), which constitutes a potential byproduct, in addition to phosphorus. Here, we focus on the Early Permian Larvik Monzonitic Plutonic Complex (LPC; Oslo Rift, Norway), which displays Fe-Ti-P-REE mineralization whose formation remains unclear. We first described the mineralogical assemblages constituting the mineralization, the surrounding larvikites as well as the contacts between the two facies. Further geochemical investigations were performed on in-situ apatite from Kodal in order to establish its trace elements composition.

1 Introduction

The Fennoscandian Shield possesses a significant amount of igneous phosphorus mineralization in carbonatite, anorthosite and alkaline-related environments (e.g. the Fen, Sokli, Siilinjarvi carbonatitic complexes, the Bjerkreim-Sokndal layered intrusion, the alkalic Raftsund intrusion and Misvaerdalen Complex; Vartiainen & Woolley 1974; Vartiainen & Vuotovesi 1980; Gautneb et al 2013; Ihlen et al 2014; Coint et al 2020; Decrée et al 2022). Some occurrences have received much interest in recent decades, such as the Bjerkreim-Sokndal layered intrusion belonging to the Rogaland Anorthositic Province, southwestern Norway. By contrast, few deposits of alkaline affinity have been studied as possible target for apatite exploitation. The 297-256 Ma Oslo Rift (southeastern Norway) hosts the youngest magmatic rocks of the Fennoscandian Shield (e.g. Sundvoll et al 1990; Neumann et al 2004; Ziegler et al 2006; Larsen et al 2008; Decrée et al 2022), including the Larvik Plutonic Complex (LPC), which contains several Fe-Ti-P mineralizations. The LPC is organized into ten successive nested monzonitic intrusive units (numbered from I to X) with decreasing saturation in silica towards the west (Figure 1; Petersen, 1978). These intrusive units crystallized early in the formation of the Oslo Rift: U-Pb ages on zircons range from 302 Ma for the oldest (I) to 288 Ma for the youngest (X) (Dahlgren et al 1998; Rämö et al 2022).

The LPC contains several occurrences of Fe-Ti-P-rich rocks, particularly in the vicinity of the younger, silica-undersaturated plutons. The most
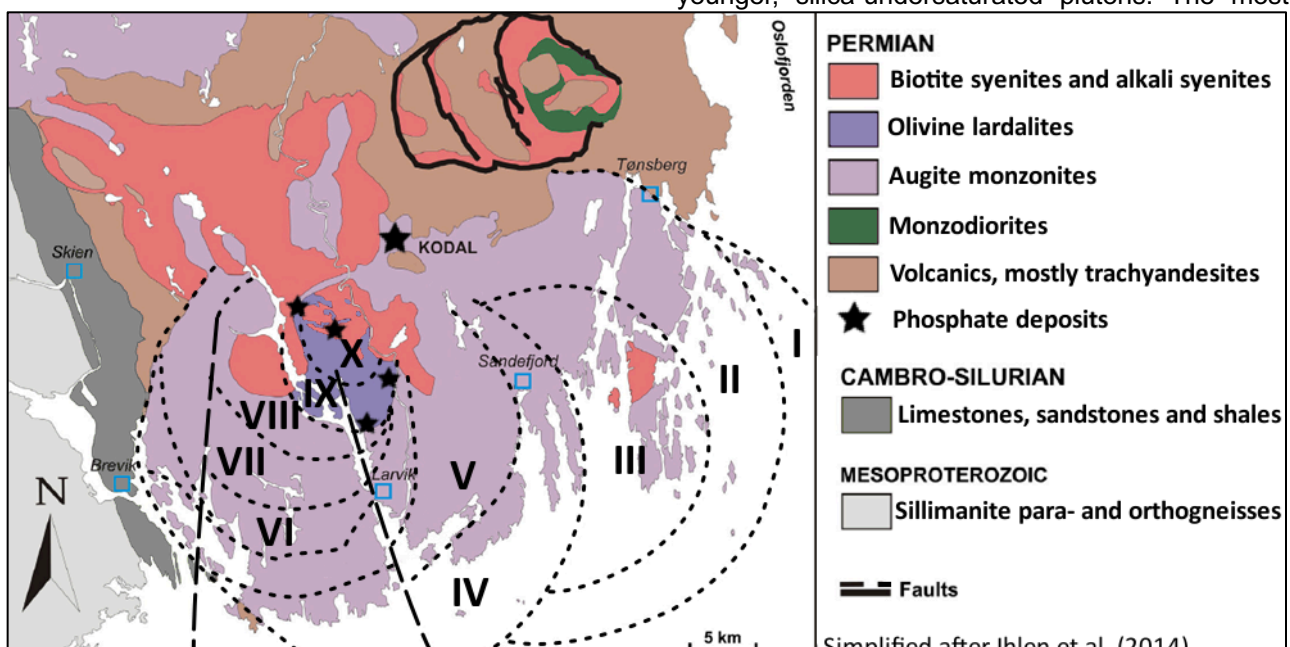

Figure 1: *Sketch map of the Larvik Plutonic Complex (LPC), SE Norway, and its subdivision into ten plutons.*

notable deposit, Kodal, occurs in an area close to the plutons V and X (Figure 1). The mineralization occurs as dyke-like lenses within the monzonite, which are ~1900 m long, a few tens of meters wide, and at least several hundred meters deep, based on previous drill cores (Ihlen et al 2014). JORC compliant resources were recently estimated at 48.9 Mt (massive and disseminated mineralization), with 4.77% P_2O_5 and 21.5% Fe (Decrée et al 2022). In addition, the Kodal mineralization also concentrates rare earth elements and yttrium (TREEY) to high levels, with mean values of ~11000 ppm TREE (Ihlen et al 2014; Decrée et al 2022). Hypotheses for the formation of the Kodal deposit include silicate-liquid immiscibility (Bergstøl 1972; Kragh & Jensen 1991), in-situ accumulation (Lindberg 1985), and accumulation in the magma chamber prior to ascent (Andersen & Seiersten 1994), but have not reached consensus.

2 Petrology and mineralogy

2.1 Fe-Ti-P-REE mineralization

The mineralization mainly consists of titanomagnetite, ilmenite and apatite, with a predominance of titanomagnetite. Other common species include silicates in various proportions, such as titaniferous augite (with Ca>Mg>>Fe>Ti) and phlogopite. Massive ore often displays plurimillimetric to centimetric Fe-Ti-P rich clusters, dominated by automorphic magnetite along the {111} or {110} crystallographic planes, with ilmenite being exsolved as lamellae in its cleavages (Figure 2A). Apatite crystallized as circular, ovoid xenomorphic crystals or as elongated prisms, with rare signs of zonation. The most massive Fe-Ti-P-REE mineralization is limited to these three mineralogical phases, but the oxides and apatite can also be intercalated between variable amounts of fractured and subhedral titanaugite (Figure 2A). Phlogopite is a common mineral, usually separating the oxides from the plagioclases in the monzonitic facies.

2.2 Monzonitic rocks of the LPC

The most common rock-type in the LPC is coarse-grained larvikites (monzonites), whose main features are rhomb-shaped feldspar phenocrysts with Schiller effect (Le Maitre 2002). Plagioclase grains are predominantly sodic (An$_{<40}$) and show a frequent antiperthitic texture. In addition to the plagioclase and alkali feldspar phenocrysts, which make up most of the volume of the larvikites, the intergranular space comprises mafic clusters similar to the mineralization (Figure 2B). Magnetite is associated with ilmenite and apatite, displaying the same textures as in the mineralization but with a greater proportion augite, hornblende and phlogopite, all bearing titanium. Pegmatitic pockets also occur, containing frequent alkaline accessory minerals: Na-bearing pyroxenes and amphiboles, zircon, baddeleyite and zirconolite-3O

$[(Ca, Y, REE)_2 Zr_2 (Ti, Nb)_3 FeO_{14}]$.

Plutons IX and X of the LPC show a higher degree of silica undersaturation, expressing as lardalites (massive nepheline syenite, with rhomb-shaped feldspars and massive, squarish nepheline crystals; Neumann 1980; Le Maitre 2002). The higher (Na+K)/Si ratio of these rocks implies a higher proportion of mafic minerals such as phlogopite, aegirine, or various Na-amphiboles.

Larvikites do not show much chemical variation throughout the successive plutons, apart from the decreasing silica-saturation, which is the main evolutionary marker: plutons I and II are oversaturated and contain quartz, whereas plutons III-VIII oscillate between quartz saturation and moderate undersaturation that shows accessory nepheline (Petersen 1978; Neumann 1980).
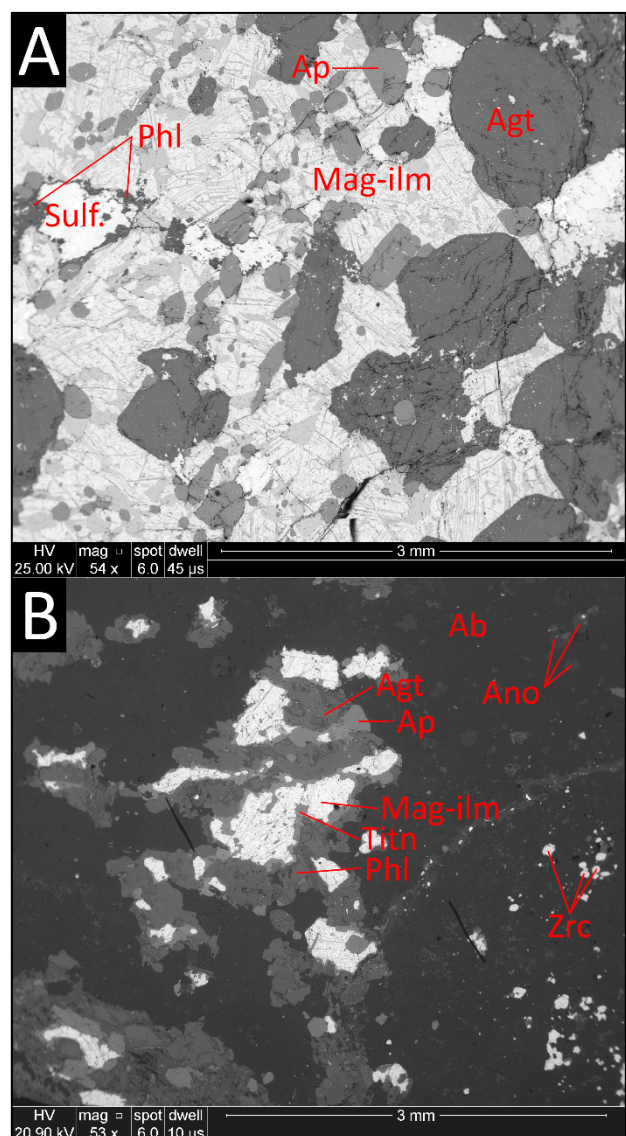
Figure 2. SEM backscatter electron pictures. A: massive mineralization of Kodal, with recurrent exsolutions of ilmenite lamellae in magnetite cleavages, and large roundish clinopyroxene grains. B: coarse-grained larvikite, very close to the disseminated ore of Kodal. Large phenocrysts of albite (top left, top right, bottom right) host minor phases and the same mineral assemblages in the intergranular space as in the mineralization. Mineral abbreviations: Ab: albite; Agt: Ti-augite; Ano: anorthoclase;

Ap: fluorapatite; Mag-ilm: magnetite and ilmenite; Phl: Ti-phlogopite; Sulf.: minor Fe-Cu sulfides; Titn: titanite; Zrc: zircon.

3 Material and methods

Priority was given to the sampling of the Fe-Ti-P-REE mineralization, especially from the Kodal deposit, which represents the most promising P_2O_5 and REE occurrences. Other lithologies sampled include nearby larvikites, larvikites from pluton V, lardalites from plutons IX and X, as well as a few other minor lithologies found in contact with the Kodal mineralization. Both mineralogical assemblages and petrographic textures were investigated in polished sections for 141 samples, using a SEM (Royal Belgian Institute of Natural Sciences).

In addition, whole-rock major and trace elements of 134 samples were analyzed at both the Laboratoire G-Time (ULB) and the Geological Survey of Norway (NGU). Major element measurements were performed using a ThermoScientific iCAP 7000 series ICP-OES (ULB) and a XRF PANalytical Axios 4kW (NGU), whereas trace elements were measured by an Agilent technologies 7700 series ICP-MS (ULB), a XRF PANalytical Axios 4kW (NGU) and a LA-ICP-MS (NGU), the latter consisting in a New Wave 193nm laser connected to a Thermo Fischer Scientific "Element XR" ICP-MS.

Trace elements composition on in-situ apatite were performed in the division of Geology, KULeuven (Belgium), as well as in NGU, in each case using a Teledyne-Cetac Analyte Excite 193 nm excimer laser coupled with an Agilent Technologies 8900 series Triple Quadrupole ICP-MS.

4 Geochemistry

4.1 Potential regarding the P mineralization

The Fe-Ti-P-REE massive mineralization of the LPC displays a very restricted mineralogy, particularly at Kodal. It includes three types of minerals: oxides (magnetite-ilmenite), silicates (titanaugite, phlogopite) and phosphates, mostly apatite. Each of these three groups preferentially concentrates distinct elements: apatite incorporates most of trace elements such as Sr and REE, due to the high difference between partition coefficients of these elements for apatite and other minerals of the mineralization (Li et al 2023). SEM investigations, combined with whole-rock elemental analyses show that apatite enrichment in the mineralization is quite variable (with whole-rock P_2O_5 content between 1.5% and 11.5%), with an average of about 6.5% P_2O_5 and about 3000 ppm TREEY. These observations suggest that the Kodal apatite contains REE in substitution on the order of 1%, in agreement with Ihlen et al (2014).

In-situ trace elements compositions from the Kodal deposit display strong enrichments in REE, particularly in LREE (Figure 3), with mean values of 11500 ppm TREEY, with an upper limit of 14700 ppm TREEY for unaltered massive mineralization. The actinide contents in apatite remain low, with typical values around 50 ppm Th and 12 ppm U. The apatite compositions obtained give the Kodal mineralization the status of potential P, REE, and F reserves (Andersen & Seiersten 1994), in a time where Europe seeks to assess its critical raw material resources.
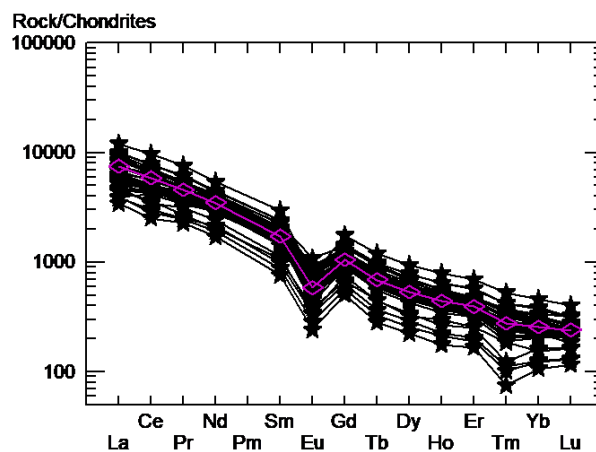

Figure 3. REE spider diagram of the apatite from the Kodal Fe-Ti-P-REE deposit (black stars), with the mean as the purple diamonds pattern. Normalized to C1 chondrites (Sun & McDonough 1989).

4.2 An onset closely related to the LPC

Whole-rock data, namely Nb/Ta and REE patterns and ratios, shows that the monzonitic rocks of the LPC share the same source as the Fe-Ti-P-REE mineralization. Moreover, the LPC plutons crystallized by successive emplacement of very similar plagioclase-rich mushes with a high Sr/Nd ratio and a positive Eu anomaly (Figure 4, A). In contrast, the mineralizations show a negative anomaly in Eu, coupled with ratios in La/Gd and Gd/Lu that differ from the range of monzonitic rocks (Figure 4, A,B). Regarding these first observations, we propose that the mineralized rocks could be a magmatic residue common to all the monzonitic plutons, dissociated in the magmatic chamber by either liquid-liquid immiscibility or fractional crystallization. Similarly to the model proposed by Andersen & Seiersten (1994), the residual P-rich magma would have ascended later, in an already emplaced and cooling larvikite.

5 Perspectives

Many questions remain, notably about the source of these mineralizations and their petrogenetic links with the LPC monzonitic rocks. Further elemental and isotopic analyses are therefore planned to bring further insights.
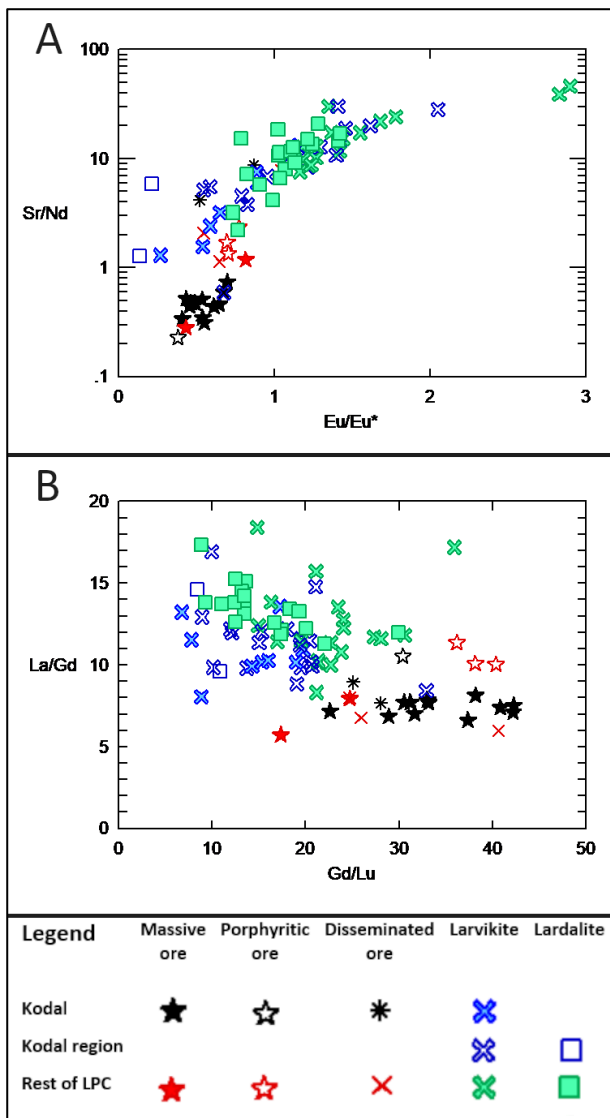
Figure 4. A : Trace element ratios underlying the enrichment of plagioclase (high Sr/Nd value, Eu/Eu*>1) for all monzonitic rocks, except for a few larvikites in and close to Kodal. B: (La/Gd) vs (Gd/Lu). Mineralizations constantly show a ratio in La/Gd distinctly lower than the range of monzonitic rock, hinting for a global segregation of the ore in the LPC. Low Gd/Lu values are believed to trace the enrichment in zircons.

Acknowledgements

References

Andersen T and Seiersten M (1994): Deep cumulates in a shallow intrusion: Origin and crystallization history of a pyroxenite (jacupirangite s.l.) body in the Larvik Pluton, Oslo Region, South Norway; in Neues Jahrbuch fur Mineralogie Monatshefte 1994-6, p. 255-274

Bergstøl S (1972): The Jacupirangite at Kodal, Vestfold, Norway: in Mineralium Deposita 1972-7, p. 233-246

Coint N, Keiding JK and Ihlen PM (2020): Evidence for Silicate-Liquid Immiscibility in Monzonites and Petrogenesis of Associated Fe-Ti-P-rich rocks: Example from the Raftsund Intrusion, Lofoten, Northern Norway; in Journal of Petrology 2020-00(0), p.1-39

Dahlgren S, Corfu F and Heaman L (1998): Datering av plutoner og pegmatitter i Larvik pluton-kompleks, sydlige Oslo Graben, ved hjelp av U-Pb isotope i zircon og baddeleyitt; in Kongsberg Mineralsymposium 1998, Norsk Bergverksmuseum Skrift, 1998-14, p. 32-39

Decrée S, Coint N, Debaille V, Hagen-Peter G, Leduc T and Schiellerup H (2022): The Potential for REEs in Igneous-related Apatite Deposits in Europe; in Geological Society, London, Special Publications 2022-526(1)

Gautneb H, Ahtola T, Lintinen P, Bergman T, Gonzalez J, Hallberg A, Litvinenko V, Shchiptsov V and Voytekhovsky YL (2013): Industrial Mineral Deposit Map of the Fennoscandian Shield 1:2.000.000; in Geological Survey of Norway; Geological Survey of Finland; Geological Survey of Sweden; SC Mineral; Institute of Geology, Karelian Research Centre, RAS; Geological Institute of the Kola Science Centre, RAS

Ihlen PM, Schiellerup H, Gautneb H and Skår Ø (2014): Characterization of apatite resources in Norway and their REE potential – A review; in Ore Geology Reviews 2014-58, p. 126-147

Kragh K and Jensen OA (1991): An immiscible iron-rich liquid in a larvikite magma?; GeoSkrifter 1991-38, p. 32-34

Larsen BT, Olaussen S, Sundvoll B and Heeremans M (2008): The Permo-Carboniferous Oslo Rift through six stages and 65 million years; in Episodes 2008-31(1), p. 52-58

Le Maitre RW (Editor), Streckeisen A, Zanettin B, Le Bas MJ, Bonin B, Bateman P, Bellieni G, Dudek A, Efremova S, Keller J, Lameyre J, Sabine PA, Schmid R, Sørensen H and Woolley AR (2002): Igneous Rocks, A Classification and Glossary of Terms; Cambridge University Press

Lindberg A (1985): Fe-Ti-P Mineralizations in the Larvikite-Lardalite Complex, Oslo Rift; in Norges Geologiske Undersøkelse Bulletins 402, p. 93-98

Li W, Costa F, Oppenheimer C and Nagashima K (2023): Volatile and trace element partitioning between apatite and alkaline melts; in Contribution to Mineralogy and Petrology 2023-178(9), 24 p

Neumann E-R (1980): Petrogenesis of the Oslo Region Larvikites and Associated Rocks; in Journal of Petrology 1980-21(3), p. 499-531

Neumann E-R, Wilson M, Heeremans M, Ann Spencer E, Obst K, Timmerman MJ and Kirstein L (2004): Carboniferous-Permian rifting and magmatism in southern Scandinavia, the North Sea and northern Germany: a review; in Geological Society, London, Special Publications 223, p. 11-40

Petersen JS (1978): Structure of the Larvikite-Lardalite Complex, Oslo-Region, Norway, and it Evolution; in Geologische Rundschau 1978-67(1), p. 330-342

Sun S-s and McDonough WF (1989): Chemical and isotopic systematics of oceanic basalts: implications for mantle composition and processes; in Geological Society, London, Special Publications 1989-42, p. 313-345

Sundvoll B, Neumann E-R, Larsen BT and Tuen E (1990): Age relations among Oslo Rift magmatic rocks: implications for tectonic and magmatic modelling; in Tectonophysics 1990-178, p. 67-87

Rämö TO, Andersen T, and Whitehouse MJ (2022): Timing and Petrogenesis of the Permo-Carboniferous Larvik Plutonic Complex, Oslo Rift, Norway: New Insights from U-Pb, Lu-Hf, and O Isotopes in Zircon; in Journal of Petrology 2022-63, p. 1-29

Vartiainen H and Woolley AR (1974): The age of the Sokli carbonatite, Finland, and some relatioships of the North Atlantic alkaline igneous province; in Bulletins of the Geological Society of Finland 1974-46, p. 81-91

Vartiainen H, and Vuotovesi T (1980): The Sokli carbonatite complex; in Lithos 1980-13, p. 224-225

Ziegler PA, Schumacher ME, Dèzes P, Van Wees J-D and Cloetingh S (2006): Post-Variscan evolution of the lithosphere in the area of the European Cenozoic Rift System; in Geological Society, London, Memoirs 32, p. 97-112

Magmatic and hydrothermal processes in a carbonatite-related REE mineralization system: insights from the Maoniuping deposit, southwestern China

Zhe Chi[1,2], Pei Ni[1], Junyi Pan[1], Zengqian Hou[3], Dawid Szymanowski[2], Cyril Chelle-Michou[2]
1State Key Laboratory for Mineral Deposits Research, Institute of Geo-Fluids, School of Earth Sciences and Engineering, Nanjing University, Nanjing, China
2 Department of Earth Sciences, ETH Zürich, Zürich, Switzerland
3 Institute of Geology, Chinese Academy of Geological Sciences, Beijing, China

Abstract. In carbonatite-related REE systems, the relative importance of magmatic and hydrothermal processes is debated. Based on our new data on high-precision zircon geochronology and in situ geochemistry from the Maoniuping REE deposit, we suggest that the giant REE mineralization may be generated from a super-enriched fluid within a short period of time. Rejuvenation of the system upon magma recharge may play an important role in REE enrichment in alkaline complexes.

1 Introduction

Carbonatites are associated with most of the REE resources in the world. However, the magmatic and hydrothermal processes in carbonatitic systems that concentrate REE elements to economic levels (wt.%) are still poorly constrained. The Cenozoic Maoniuping deposit, China, displays a clear mineralization zonation, a well-established intrusion sequence, and limited supergene alteration, providing an outstanding case study to decipher the magmatic and hydrothermal processes for REE mineralization.

In this study, we obtained high-precision U-Pb zircon ages from pre- and post-ore intrusions, with the aim of constraining the duration of magmatic-hydrothermal ore formation. Spatially resolved geochemical information from zircon core and rim was collected to track the magmatic processes involved in the formation of REE mineralization. Additionally, REE concentration of fluids was obtained by LA-ICP-MS analysis of fluid inclusions in fluorite and quartz, which are closely associated with the ore mineral (bastnaesite). These data were included in a mass balance calculation to examine the REE mineralization lifespan determined by geochronology.

## 2 Geology of the Maoniuping deposit

The Maoniuping deposit, located in the western Yangtze craton, is the fifth largest REE mineralization in the world. It contains resources of 3.17 Mt REO with an average grade of 2.95 wt.%. It is hosted in an Oligocene syenite-carbonatite complex formed in a post-collisional environment.

The REE mineralization is centred around a composite alkaline intrusion made of lamprophyre dykes, quartz syenite pluton, carbonatite dykes, and alkaline granite porphyry (Fig. 1A). Syenitic plutonic

rocks were emplaced first, followed by the intrusion of lamprophyre dykes. Ore-related carbonatite intruded into syenite and lamprophyre dykes, resulting in extensive fenitization superimposed on the earlier-formed magmatic rocks (Fig. 2A-E). Granite porphyry crosscuts all early intrusions and ore veins (Fig. 2F-G), representing the latest magmatic pulse.
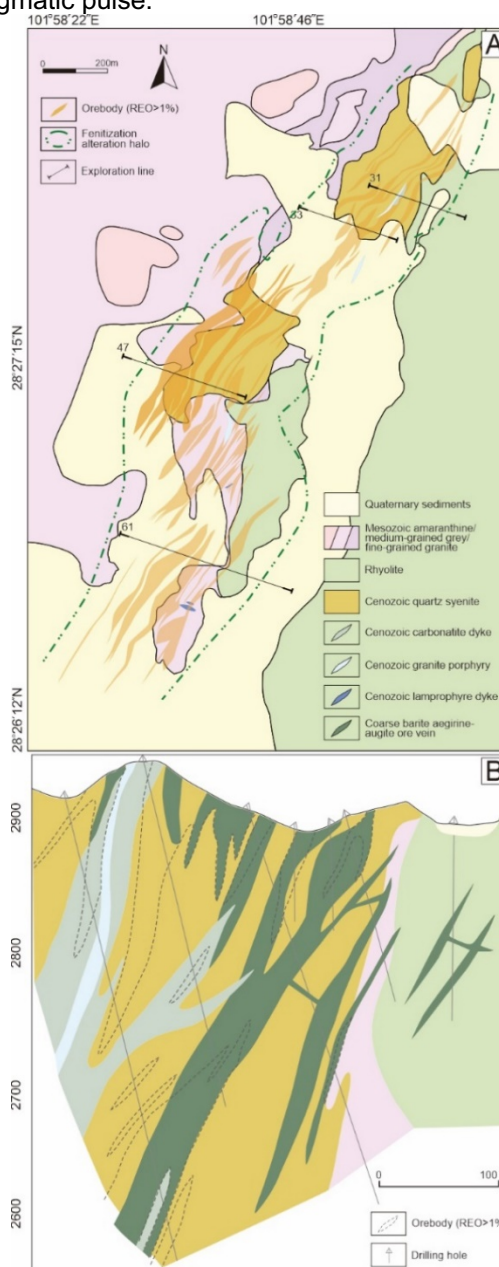
Figure 1. (A) Simplified geologic map showing the distribution of carbonatite-alkaline complexes and REE orebodies in the Maoniuping deposit (modified after Yuan et al. 1995); (B) Cross-section along exploration line 31 (modified after Yuan et al. 1995).
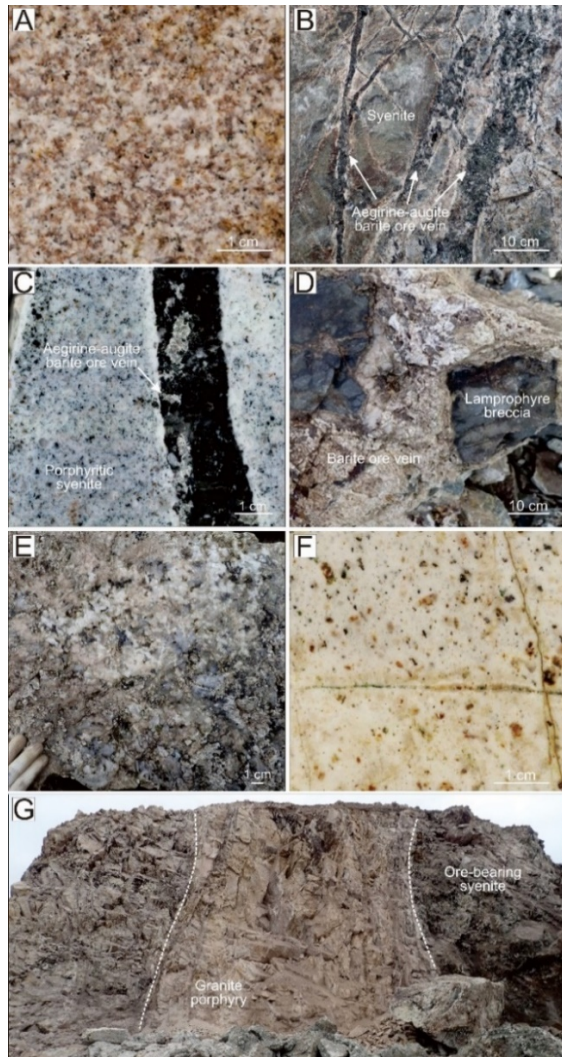
Figure 2. (A) Quartz syenite; (B) Aegrine-augite barite REE ore stockwork veins hosted in the syenite; (C) Aegrine-augite barite ore veins cutting porphyritic syenite; (D) Lamprophyre breccia in barite REE ore veins; (E) Pink calcite carbonatite with fluorite and barite; (F) Barren granite porphyry; (G) Barren granite porphyry intruding quartz syenite and cutting ore stockwork veins

The majority of the REE mineralization is hosted in two types of ore veins: aegirine-augite-barite stockwork veins (Fig. 1 B and C) and carbonatitic veins and dykes (Fig. 1E). These two types of veins are composed of broadly similar mineral assemblages but different mineral ratios, including aegirine-augite, feldspar, arfvedsonite, calcite, bastnaesite, quartz, fluorite, barite, and exhibit similar trending orientations at the deposit scale. At the location where carbonatite dyke is exposed, there is a transition from carbonatite veins to aegirine-augite-barite veins, indicating that both mineralization styles are generated by a single fluid pulse.

3 Samples and Methodology

One sample of pre-ore syenite (MNP018) and two samples of post-ore granite porphyry (MNP017 and MNP049) were collected. In situ LA-ICP-MS measurements and chemical abrasion-isotope dilution-thermal ionization mass spectrometry (CA-ID-TIMS) analysis were performed at ETH Zurich. The separated zircons were annealed for 48 h at 900 ℃, and then were mounted in epoxy. Polished zircons were imaged using SEM-CL, followed by in situ LA-ICP-MS analysis for trace elements and U-Pb isotopes. Based on the in-situ zircon compositions and the CL texture, some grains were plucked out of the mounts and processed for high-precision U-Pb analyses by CA-ID-TIMS.

Fluid inclusions in quartz and fluorite were analyzed by LA-ICP-MS at the fluid inclusion lab at Nanjing University to obtain their major and trace elemental compositions. The detailed procedure refers to the description by Pan et al. (2019). The sulfate concentrations of fluid inclusions were used as internal standards, which are obtained by combining microthermometric data with a calibrated sulfate solubility curve (Chen et al. 2020).

4 Timescales of ore formation: bracketed by the dates of pre-ore and post-ore intrusions

Previous in situ geochronology indicated that the magma evolution and REE mineralization of the Maoniuping syenite-carbonatite complex occurred over 2.5 Myr (Weng et al. 2020). Our new high-precision U-Pb dates of individual zircon crystals do not reveal a prolonged magmatic history but suggest a highly constrained magmatism and mineralization timescale (Fig. 3). The youngest zircons from each sample are interpreted as the closest approximation of the emplacement age of each intrusion. These youngest zircons in pre- and post-ore intrusions bracket the maximum duration of ore formation to a time interval of ca. 0.15 Myr.
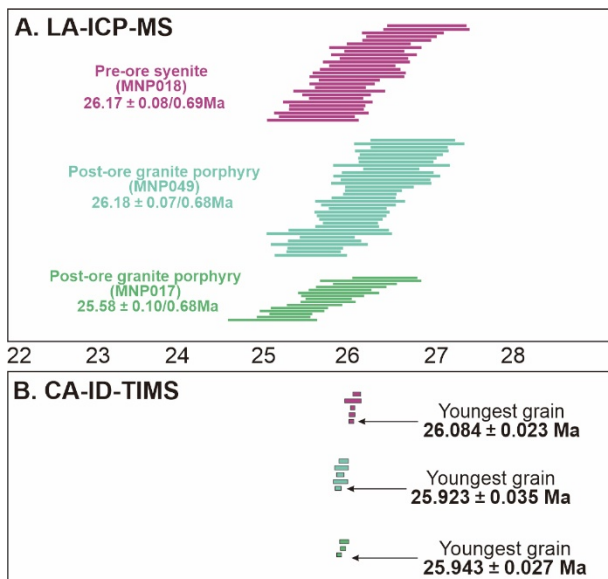
Figure 3. Geochronology of the Maoniuping magmatic system. (A) Ranked LA-ICP-MS $^{206}Pb/^{238}U$ dates. Weighted mean ages are given with two uncertainties: (1) 2σ internal uncertainty and (2) with propagated external uncertainty; (B) Ranked CA-ID-TIMS $^{206}Pb/^{238}U$ dates with date and uncertainty of the youngest zircons.

The fluid inclusions hosted in bastnaesite and associated minerals (quartz and fluorite) are polycrystalline inclusions, with sulfate and a small amount of carbonate as daughter minerals. REE concentrations of fluid inclusions in quartz and fluorite associated with bastnaesite ranged from 1070 to 17200 ppm, with an average of 4000 ppm. Mass balance calculation shows that assuming a maximum mineralization duration of 0.15 Ma, the fluid flow rate will be 0.15 kg/s. While it is on the low end of what has been reported in geothermal systems and hot springs (0.1 to 1000 kg/s, Moncada et al. 2019), the mineralizing pulse may have been much shorter than the bracketed interval duration, thereby allowing for higher fluid flow rates.

5 Magmatic processes: insights from zircon chemistry in pre-ore syenite

Four zircon CL textural categories were devised to classify the grains observed (Fig. 4). A-type zircon displays grey continuous oscillatory zoning. B-type zircon is characterized by a bright CL texture. C type has a core-rim texture with resorption textures on the core. D-type zircons contain rims with dark luminescence.

The LA-ICP-MS dates of the four types of zircon are overlapping. From core to rim, A-type zircon grains usually display a trend of declining Th/U ratio (Fig. 4A and B), indicating a fractionating trend jn the presence of co-crystallizing titanite and apatite (both abundant minerals in the magmatic rocks of Maoniuping). The REE content in A-type zircons usually decreases from core to rim (Fig. 4A). B-type zircon grains have the highest Th/U ratio and Ti content, and lowest Yb/Gd$_N$ ratio (Fig. 4C and D). Most C-type zircon grains show a rejuvenation trend,

manifested by decreased Th/U ratios and increased Yb/Gd$_N$ ratios (Fig. 4E and F). In C-type zircons, the REE contents are generally higher at the rim (Fig. 4E). The dark rims of D-type zircons are characterized by elevated Hf concentrations and often display more evolved Yb/GdN and Th/U ratios (Fig. 4G and H).

The appearance of high-temperature and low-evolution B-type zircons and the tendency of C-type zircons to become less evolved from core to rim pinpoints toward magma recharges into the syenitic magma reservoir. As recorded in A-type zircons, magmas are progressively depleted in REE content as apatite and titanite crystallize. The less-evolved rims of C-type zircons usually have enriched REE contents compared to the core suggesting that the rejuvenation the magmatic system may contribute to the REE enrichment in alkaline complexes.
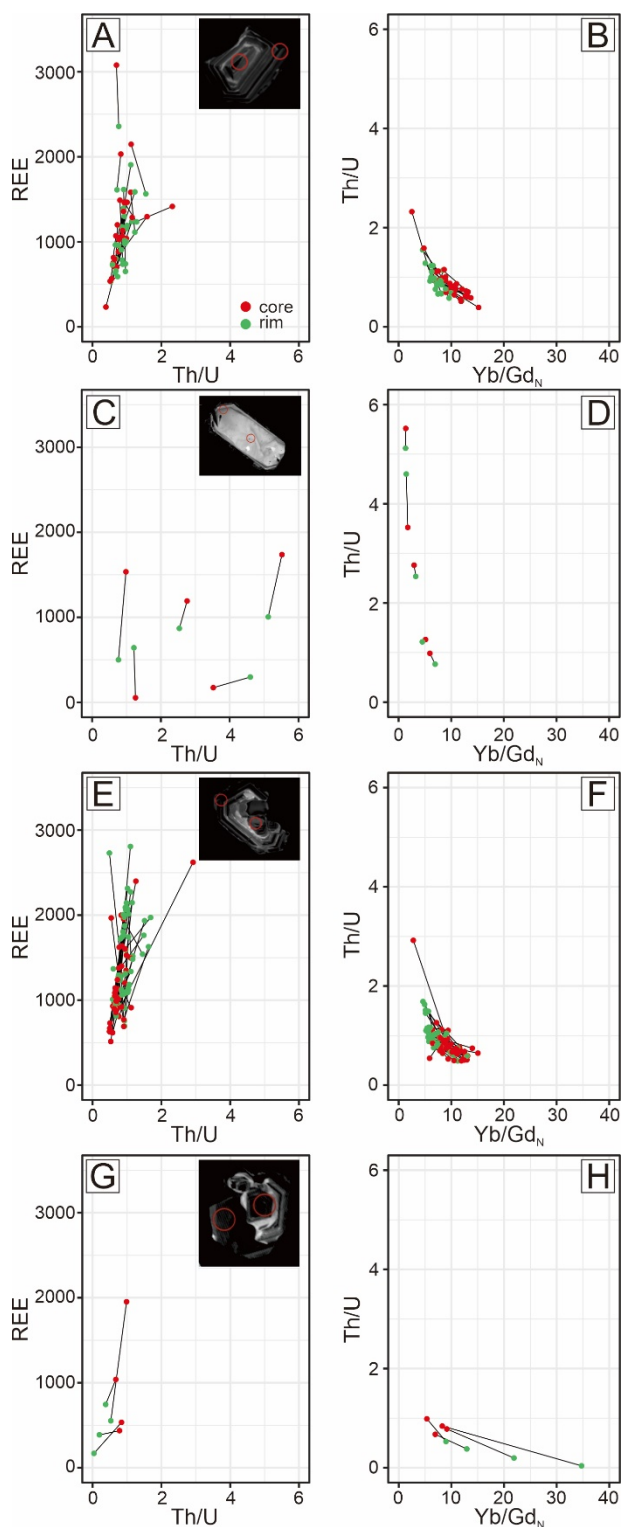
Figure 4. REE vs Th/U and Th/U vs Yb/Gd$_N$ trends from core to rim for each type zircons. (A-B) A-type; (C-D) B-type; (E-F) C-type; (G-H) D-type.

Pan JY, Ni P, Wang RC (2019) Comparison of fluid processes in coexisting wolframite and quartz from a giant vein-type tungsten deposit, South China: Insights from detailed petrography and LA-ICP-MS analysis of fluid inclusions. AM MINERAL 104(8):1092-1116.

Weng Q, Yang WB, Niu HC, Li NB, Mitchell RH, Zurevinski S, Wu D (2022) Formation of the Maoniuping giant REE deposit: Constraints from mineralogy and in situ bastnäsite U-Pb geochronology. AM MINERAL 107(2): 282-293.

Yuan ZX, Shi ZM, Bai G, Wu CY, Chi RA, Li XY (1995) The Maoniuping rare earth ore deposit, Mianning County, Sichuan Province. Seismological Publishing House: Beijing 150 (in Chinese).

References

Chen H, Cui H, Zhong R, Xie Y, Yu C, Li Z, Ling Y (2020) Solubility of Na_2SO_4 in silica-saturated solutions: Implications for REE mineralization. AM MINERAL 105(11):1686-1694.

Moncada D, Rimstidt JD, Bodnar RJ (2019) How to form a giant epithermal precious metal deposit: Relationships between fluid flow rate, metal concentration of ore-forming fluids, duration of the ore-forming process, and ore grade and tonnage. ORE GEOL REV 113:103066.

Dating multi-stage REE mineralization in Canada: the example of Thor Lake and Saint Honoré deposits

Hélène Legros[1,2,3], D. Graham Pearson[3], Sarah Dare[2], L. Paul Bédard[2]
[1]*Ministère des Ressources Naturelles et des Forêts, Gouvernement du Québec, Canada*
[2]*Department of applied sciences, CERM, Université du Québec à Chicoutimi, Chicoutimi, Canada*
[3]*Department of Earth and Atmospheric Sciences, University of Alberta, Edmonton, Canada*

Abstract. Geochronology applied to ore deposit geology is in constant development and aims to better define the timing of deposition of potential targets, and help to constrain petrogenetic models available for exploration. In the case of REE deposits, alkaline and carbonatite plutonic suites are generally targeted. However, many magmatic REE deposits are remobilized by late hydrothermal processes that could affect endowment. Therefore, it is crucial to constrain the timing of both magmatic and regional hydrothermal ore events. Here, we show results for the Thor Lake bastnaesite mineralization (Slave craton) and the apatite grains of Saint Honoré (Saguenay-Lac-Saint-Jean, Québec).

1 Introduction

REE resources are critical in most areas of the world due to the increasing demand for the development of new technologies (Dushyantha et al. 2020). Our understanding of ore deposition is linked to our understanding of the timing of formation.

Direct dating of ore minerals is not always possible due to the lack of proper matrix-match reference material. However, in the past decades, there has been an increasing interest in developing ore mineral reference materials for geochronology purposes and specifically, U-Pb dating.

Here, we focus on two REE-bearing minerals: one with major REE concentrations, bastnaesite ($(La,Ce,Y)CO_3F$), and one with trace or minor amount of REE, apatite ($Ca_5(PO_4)_3(F,Cl,OH)$).

Both minerals currently have at least one reference material available in the literature. However, both minerals show very low U concentrations and variable common Pb concentrations, which make acquisition as well as data processing challenging (Chew et al. 2014; Roberts et al. 2020).

Precise dating of these minerals is crucial to investigate mineralizing processes, also to define what the lifetime of these processes is. Most REE deposits are emplaced in association with a major magmatic event but exhibit replacement textures indicative of late hydrothermal remobilization of the minerals. Direct dating could highlight the eventual time gap between these two endowment events.

2 Preliminary results

2.1 Bastnaesite dating

Bastnaesite grains were selected from the world-class Thor Lake deposit, located in the Slave Craton in Canada. The analyses were done at the University of Alberta using an iCAP. No matrix-match reference material was available in the Archean age range; therefore, the analyses were run with two reference materials: the K9 bastnaesite and the WC-1 marine calcite. The K9 Bastnaesite is dated at ca. 116 Ma while WC-1 is dated at ca. 254 Ma. The alkaline plutonic suite associated with the Thor Lake mineralization is Mesoarchean (ca. 2.2 Ga).

The Thor Lake bastnaesite has concentrations of U from 0 to 10 ppm, Pb from 40 to 140 ppm and Th from 200 to 800 ppm. The low U concentration is a common feature of carbonate minerals (Roberts et al. 2020). The variation in U-Pb-Th in the bastnaesite grains is controlled by the zoning and the alteration of the grains into parasite, which is easily trackable with the elevation of the Ca concentration.

The first results show a spectrum of ages ranging from sub-concordant 2.0 Ga ages, close to the magmatic event, to ca. 1.77 Ga for the unaltered bastnaesite. However, altered grains give ages as young as 865 Ma. The meaning of such a large age gap and correspondence to regional events is currently being discussed.

2.2 Apatite dating

Apatite is a ubiquitous mineral in ore deposits (Webster and Piccoli 2015). We selected grains from various alkaline and carbonatite REE-Nb mineralization targets located in the Québec province in Canada (such as Saint- Honoré). Apatite has been the subject of U-Pb geochronology development, which is still being developed thanks to analytical advancements of ICP-MS, notably the LA-ICP-MS/MS mode. One of the main limitations of apatite U-Pb dating is the substantial amounts of initial (non-radiogenic, or common) Pb compared to U when it crystallizes (Chew and Spikings 2015), which leads to substantial Pb correction (Chew et al. 2014). LA-ICP-MS/MS mode allows to precisely correct common lead by removing the interference with Hg.

The apatite grains from the carbonatite of Saint-Honoré were analysed along with MAD and Durango reference material on an ICP-QQQ-MS at the Université du Québec à Chicoutimi. The large grain size and abundance of the samples allows us to acquire a substantial dataset that will document the timing of ore deposition for the first time. Several apatite textures are observed: disseminated, disseminated oriented, radial aggregated and in veins. These textures hint at distinct magmatic-

hydrothermal events consistently with observations made by previous studies (Néron et al. 2018). This study aims to date these events but also to document the potential reopening of the U-Pb system in apatite in different magmatic-hydrothermal conditions.

Acknowledgements

References

Chew DM, Petrus JA, Kamber BS (2014) U–Pb LA–ICPMS dating using accessory mineral standards with variable common Pb. Chemical Geology 363:185–199. https://doi.org/10.1016/j.chemgeo.2013.11.006

Chew DM, Spikings RA (2015) Geochronology and thermochronology using apatite: time and temperature, lower crust to surface. Elements 11:189–194

Dushyantha N, Batapola N, Ilankoon I, et al (2020) The story of rare earth elements (REEs): Occurrences, global distribution, genesis, geology, mineralogy and global production. Ore Geology Reviews 122:103521

Néron A, Bédard LP, Gaboury D (2018) The Saint-Honoré carbonatite REE zone, Québec, Canada: Combined magmatic and hydrothermal processes. Minerals 8:397–397

Roberts NMW, Drost K, Horstwood MSA, et al (2020) Laser ablation inductively coupled plasma mass spectrometry (LA-ICP-MS) U–Pb carbonate geochronology: strategies, progress, and limitations. Geochronology 2:33–61. https://doi.org/10.5194/gchron-2-33-2020

Webster JD, Piccoli PM (2015) Magmatic apatite: A powerful, yet deceptive, mineral. Elements 11:177–182

Stable isotope constraints on the source of ore fluids for the Hicks Dome REE+Y-HFSE-fluorspar deposit

Julia A. McIntosh[1], Craig A. Johnson[1], Allen K. Andersen[2], Albert H. Hofstra[1]
[1] *U.S. Geological Survey, Denver CO, USA*
[2] *U.S. Geological Survey, Spokane WA, USA*

Abstract. Hicks Dome is comprised of coarse crystalline Mississippi Valley Type deposits at shallow levels and an enigmatic, fine-grained fluorite, rare earth elements, Y, high field strength elements, Be, and Ba rich deposit at deeper levels. Phyllosilicates from a lamprophyre dike and a breccia from two Hicks Dome drill cores were sampled to resolve the fluid history of the entire deposit using light stable isotopes. Silicate fluorination coupled with isotope ratio mass spectrometry give $\delta^{18}O$ values from +6.9 to +16.0 ‰ (Vienna Standard Mean Ocean Water). Temperature conversion elemental analyzer and gas chromatography-isotope ratio mass spectrometry give δ^2H values from -54 to -33 ‰ (Vienna Standard Mean Ocean Water). Muscovite from metasomatized dikes and breccias are relatively enriched in ^{18}O compared to phlogopite from lamprophyre. Calculated isotopic compositions of the fluids from which the phyllosilicates precipitated indicate that phlogopite retained a magmatic composition while muscovite likely formed from magmatic fluids that exchanged with carbonate host rocks or from magmatic fluids that mixed with basinal brines. Enrichment of deuterium in fluids calculated from muscovite suggest that fluids were derived from hypothesized carbonatites or were acidic. These data demonstrate that the Hicks Dome critical mineral resource is magmatic hydrothermal in origin.

1 Introduction

The Illinois-Kentucky Fluorspar District (IKFD) in the midcontinent region of the USA (Figure 1) is comprised of fluoritic Mississippi Valley-Type (MVT) Pb-Zn deposits. Previous studies of coarsely crystalline fluorite, barite, and Pb-Zn deposits have suggested that the ores formed from basinal brines that migrated northward from the Arkoma Basin in response to uplift of the Alleghanian-Ouachita orogenic belt during the late Paleozoic (Figure 1; Plumlee et al. 1995; Denny et al 2008). The abundant fluorine is hypothesized to be magmatic, derived either from melts related to locally abundant lamprophyre dikes that were emplaced during the Permian (Denny et al. 2008), or from a carbonatite intrusion that is thought to underlie Hicks Dome in the southern IKFD (Figure 1; Andersen et al. 2021).

The deposit at Hicks Dome differs from other fluorspar Pb-Zn deposits in the IKFD in that it is 600 m lower in the stratigraphic section and has high concentrations of numerous elements and minerals on the current U.S. Geological Survey (USGS) list of critical mineral commodities (U.S. Geological Survey 2022). The estimated resource is 65.8 million tons containing critical 15.8% fluorspar, 4.8% barite, 0.16% Be, 1.3% TiO_2, 0.2% Nb_2O_5, and 0.3% rare earth elements plus Y (REEs+Y; Andersen et al. 2021). It has been hypothesized that the Hicks

Dome deposit formed from a combination of magmatic and basinal brines following a cryptoexplosive event (e.g., Denny et al. 2008). However, incomplete understanding of the deposit paragenesis and geochemistry renders this hypothesis difficult to test (Andersen et al. 2021).
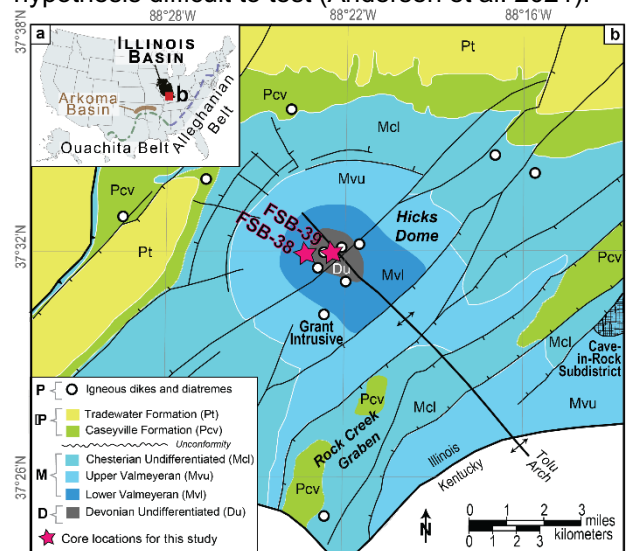
Figure 1. a. Geographic location of the Illinois basin, Alleghanian-Ouachita orogenic belt, and Arkoma basin; b. Geologic map of the Hicks Dome study area. Modified from Denny et al. (2008).

Here we present a new dataset of the oxygen and hydrogen isotopic composition of phyllosilicates in lamprophyre dikes and breccias from Hicks Dome. $\delta^{18}O$ and δ^2H values of phyllosilicate minerals precipitated from a fluid will vary systematically depending on physiochemical conditions and the $\delta^{18}O$ and δ^2H values of the associated fluid. By measuring the $\delta^{18}O$ and δ^2H values of phyllosilicates in the igneous and hydrothermally altered rocks, we can reconstruct the isotopic compositions of fluids involved in the formation of the critical mineral resource at Hicks Dome and test the hypotheses that have been raised regarding fluid sources.

2 Materials and methods

2.1 Core samples

The two drill cores examined in this study (Figure 1b) contain a lamprophyre dike (core FSB-38; Figure 2a–d) and a calcite cemented breccia (core FSB-39; Figure 2e,f). Dike and breccia samples were obtained from depths between 967–982 m, and 404–408 m below the surface, respectively. Samples were disaggregated using a mortar and pestle or

Selective Fragmentation (SelFrag), and then sieving. Phyllosilicates were separated from Ti oxides, sulfates, sulfides, and bertrandite by density separation and from quartz by hand picking.
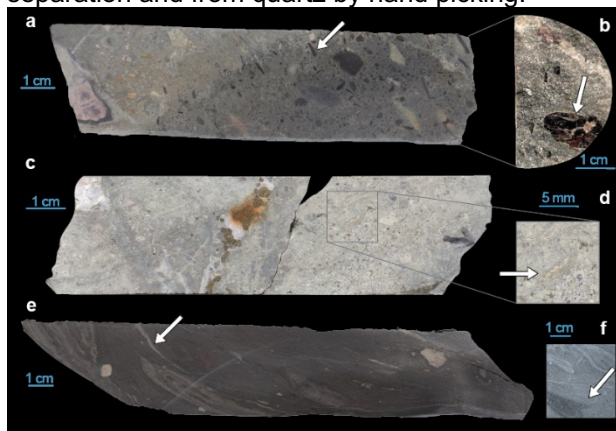
Figure 2. Photographs of drill core sampled for this study. A. Lamprophyre dike from core FSB-38, 982 m depth; b. Example of a phlogopite; c. Altered lamprophyre dike from core FSB-38, 970 m depth; d. Example of a muscovite; e. Calcite cemented breccia from core FSB-39; f. Example of muscovite. Arrows point to phyllosilicates.

Phlogopite occurs in unaltered portions of the lamprophyre dike (Figure 2b) whereas muscovite is present in metasomatized portions (Figure 2d). Phyllosilicates separated from the calcite cemented breccia were also muscovite (Figure 2f).

2.2 Stable isotopic methods

A portion of the mineral separates were reacted with BrF_5, and the resulting oxygen converted to CO_2 gas using a silicate fluorination extraction line (method of Clayton and Mayeda 1963). Oxygen isotopic analyses were completed using a Micromass Optima isotope ratio mass spectrometer (IRMS) at the USGS in Denver.

The second portion of each separate was loaded into Ag capsules and decomposed in a Thermo Temperature Conversion Elemental Analyzer (TC/EA). Evolved H_2 gas was purified by gas chromatography and analyzed for hydrogen isotopes using a Thermo Delta V IRMS at the USGS in Denver (method of Sharp et al. 2001).

Oxygen and hydrogen isotope ratios are reported in conventional delta notation in units of per mil (‰), as follows: $\delta R = ((R_{sample}/R_{standard}) - 1) \times 1000$, where R is the isotopic ratio of $^{18}O/^{16}O$ or $^2H/^1H$. The reference standard used herein is Vienna Standard Mean Ocean Water (V-SMOW). Data were normalized so that analyses of reference materials NBS 28 silica gave a $\delta^{18}O$ value of 9.58 ‰ and analyses of USGS 57 and USGS 58 gave δ^2H values of -91.5 and -28.4 ‰, respectively. Analytical error was ±0.2‰ for oxygen and ±1 ‰ for hydrogen.

Isotopic compositions of fluids were calculated from the measured phyllosilicate compositions and the empirically or experimentally derived mineral-H_2O fractionation factors of O'Neil and Taylor (1969), Suzuoki and Epstein (1976), Bowers and Taylor (1985), and Zheng (1993).

3 Results

3.1 Measured phyllosilicates

Phlogopite from the unaltered lamprophyre dike give $\delta^{18}O$ values of 6.9 to 8.6 ‰ (V-SMOW; Figure 3). Muscovite from the altered dike give $\delta^{18}O$ values of 14.9 and 16.0 ‰ whereas those from the breccia give $\delta^{18}O$ values of 13.3 and 14.1 ‰.
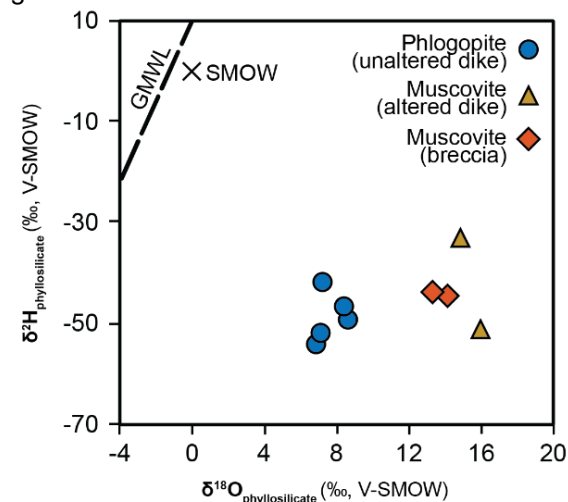

Figure 3. $\delta^{18}O$ and δ^2H (‰, relative to V-SMOW) of Hicks Dome phyllosilicates. GMWL= Global meteoric water line (Craig 1961).

Phlogopite from the unaltered lamprophyre dike give δ^2H values of -54 to -42 ‰ (V-SMOW; Figure 3). Muscovite from the altered dike give δ^2H values of -51 and -33 ‰, whereas those from the breccia give δ^2H values of -45 and -44 ‰.

3.2 Calculated fluid compositions

Phlogopite compositions measured herein are normal for ultramafic igneous rocks (e.g., Taylor and Sheppard 1986). If lamprophyre melts exsolved an aqueous fluid phase, the composition of that fluid phase would have reflected isotopic equilibrium exchange with melt and crystals near liquidus temperatures, which were probably around 1000°C. Assuming an equilibration temperature of 1000°C, calculated $\delta^{18}O_{H_2O}$ values from phlogopite in the unaltered lamprophyre dike are 9.2 to 10.7 ‰, with an average of 9.9 ‰ (Figure 4). $\delta^2H_{H_2O}$ values calculated from phlogopite in the unaltered lamprophyre dike are -66 to -54 ‰, with an average of -61 ‰ (Figure 4).

The relatively coarse (0.25–5 mm) crystalline muscovite in the metasomatized dike and calcite cemented breccia are likely precipitated from a hydrothermal fluid at temperatures between 200 to 600°C. The $\delta^{18}O_{H_2O}$ values calculated from muscovite are 5.4 to 14.6 ‰ and 3.8 to 12.8 ‰ for the altered dike and breccia, respectively (Figure 4). $\delta^2H_{H_2O}$ values calculated from muscovite are -60 to -10 ‰ and -53 to -21 ‰ for the altered dike and breccia, respectively (Figure 4).
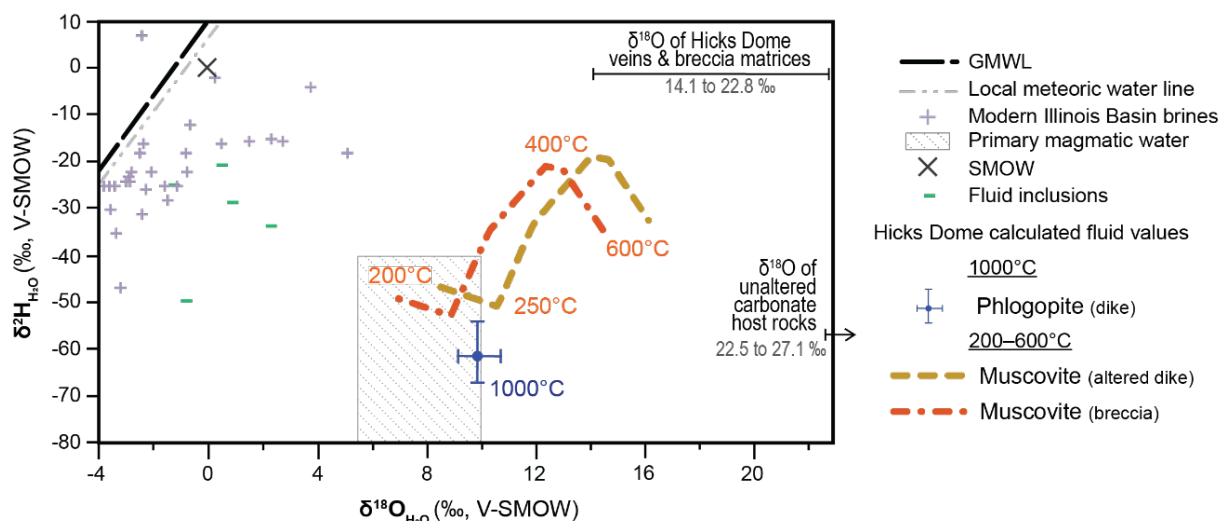
Figure 4. *Average $\delta^{18}O$ and δ^2H of calculated fluids over a range of temperatures relative to other fluid and rock compositions. Illinois Local meteoric water line from Kendall and Coplen (2001). Illinois Basin brine data from Clayton et al. (1966) and Labotka et al. (2015). Fluid inclusion data from Richardson et al. (1988). Illinois basin unaltered carbonate data from Pinckney and Rye (1972) and Moorehead (2013). Hicks Dome data from Moorehead (2013).*

4 Discussion

The $\delta^{18}O$ and δ^2H values of phlogopite from the lamprophyre dike measured herein preserve their primary magmatic compositions. This is demonstrated by the fact that their calculated fluid compositions are consistent with primary magmatic water at 1000°C (Figure 4). However, the two phlogopite samples with the most positive $\delta^{18}O$ values lie slightly outside the primary magmatic water box, which may implicate a more ^{18}O rich fluid component (Figures 3,4).

The measured $\delta^{18}O$ values of muscovite from the altered lamprophyre dike and calcite cemented breccia are more enriched in ^{18}O, which is typical of minerals that precipitate from fluids that are enriched in ^{18}O relative to meteoric water (Figure 4). If muscovite equilibrated isotopically at temperatures below 250°C, the calculated fluid compositions are consistent with mixing of a magmatic fluid related to lamprophyre emplacement, represented by the composition of $\delta^{18}O_{H_2O}$ and $\delta^2H_{H_2O}$ derived from phlogopite at 1000°C, and a basinal brine. This fluid composition supports the magmatic fluid-brine mixing model suggested by Plumlee et al. (1995). Modern brines in strata of the Illinois basin are a combination of connate water, residual brine produced by evaporation of seawater, halite dissolution brine, and meteoric water (Figure 4; Clayton et al. 1966; Labotka et al. 2015). Permian residual brines extracted from fluid inclusions in MVT fluorite and sphalerite in the Cave-in-Rock subdistrict of the IKFD (Figure 1b) are thought to represent main stage saline fluids (Figure 4; Richardson et al. 1988).

On the other hand, if muscovite equilibrated isotopically at temperatures above 250°C, the calculated fluid compositions are consistent with isotopic exchange with a magmatic fluid and Illinois basin carbonate rocks which have $\delta^{18}O$ values

between +22.5 to +27.1 ‰ (Pinckney and Rye 1972; Moorehead 2013).

Although the isotopic equilibration temperature for hydrothermal muscovite is not precisely known, the calculated $\delta^2H_{H_2O}$ value is higher than the corresponding value for the lamprophyre fluid no matter what temperature is assumed for equilibration (Figure 4). Thus, the muscovite did not form from pristine lamprophyre fluid. However, a magmatic origin for the muscovite fluid is not ruled out because a carbonatite melt could have evolved a more ^2H-enriched fluid than the lamprophyre melt.

A carbonatite source for hydrothermal fluids at Hicks Dome has been suggested due to its enrichment in REE+Y, Th, Ti, Nb, and F, which parallels that of sediment host mineralization on the periphery of the Bear Lodge carbonatite (Wyoming, USA; Andersen et al. 2021). Moreover, Moorehead (2013) measured the $\delta^{13}C$ and $\delta^{18}O$ values of calcite in veins and breccia matrices at Hicks Dome and determined that these values reflect magmatic-hydrothermal fluids that isotopically exchanged with carbonatite and Illinois basin host carbonate rocks. Lastly, Bradbury and Baxter (1992) characterized the nearby Grant Intrusive (Figure 1b) as a carbonatitic breccia, whose carbon and oxygen isotope compositions may indicate exchange between magmatic fluid and carbonate rock (Moorehead 2013).

$\delta^2H_{H_2O}$ values ≥-40‰ are not uncommon for fluids condensed from magmatic vapors. Studies have found that aqueous fluids exsolved from melts are enriched in deuterium relative to the water dissolved in the melt. Separated vapor is further enriched in deuterium relative to conjugate hypersaline brine (Giggenbach 1992). The large volume of solution collapse breccias at Hicks Dome is consistent with a magmatic fluid origin because magmatic vapors are often acidic and therefore

corrosive to carbonate rock due to high concentrations of H_2CO_3, H_2SO_4, and HCl.

It is also possible that the high δ^2H_{H2O} values are secondary, as hydrogen isotopes values are more easily modified than oxygen isotope values in phyllosilicates without phase changes and at low temperature ($\leq 350°C$; O'Neil and Kharaka 1976). This may be why the oxygen isotope values of the muscovite are similar, whereas the hydrogen isotopes show one value that is ~20 ‰ heavier than the other values (Figure 3). Deuterium rich meteoric water or Illinois basin formation water may have migrated into basement rocks under low water/rock conditions, or shale membrane filtration.

The data and calculated fluid compositions presented here suggest that there were at least two episodes of phyllosilicate formation or alteration associated with, first, intrusion of lamprophyre melts (magmatic), and second, metasomatism of the lamprophyre dikes plus breccia formation associated with the inferred intrusion of carbonatite melts (orthomagmatic and metasomatic).

5 Summary

Stable isotope data on phlogopite from a lamprophyre dike and muscovite from a metasomatized dike and calcite cemented breccia have distinct compositions. At magmatic temperatures, phlogopite from an unaltered lamprophyre dike likely formed from primary magmatic water. Enrichment in ^{18}O for calculated $\delta^{18}O_{H2O}$ values from muscovite suggests that at these minerals formed from magmatic fluids that exchanged with the carbonate host rocks or from mixing between magmatic fluids and basinal brines. High δ^2H_{H2O} values calculated from muscovite indicate they did not form from a lamprophyre fluid but may be from a carbonatite or acidic fluid with condensed magmatic vapors.

Future work will entail analyzing more phyllosilicate separates from dikes and breccias for their oxygen and hydrogen isotope ratios, and further evaluate the magmatic hydrothermal system at Hicks Dome.

Acknowledgements

References

Andersen AK, Hofstra AH, Nuelle LM (2021) Hydrothermal HFSE(+HREE) mineralization in the Bear Lodge Alkaline Complex—a key to understanding the larger Hicks Dome critical mineral resource? Goldschmidt2021 Virtual Conference

Bowers TS, Taylor Jr. HP (1985) An integrated chemical and stable-isotope model of the origin of Midocean Ridge Hot Spring Systems. Journal of Geophysical Research: Solid Earth 90:12583–12606

Bradbury JC, Baxter JW (1992) Intrusive breccias at Hicks Dome Hardin County, Illinois. Illinois State Geological Survey, Champaign, IL

Clayton RN, Mayeda TK (1963) The use of bromine pentafluoride in the extraction of oxygen from oxides and silicates for isotopic analysis. Geochimica et Cosmochimica Acta 27:43–52

Clayton RN, et al (1966) The origin of saline formation waters: 1. Isotopic composition. Journal of Geophysical Research 71:3869–3882

Craig H (1961) Isotopic Variations in Meteoric Waters. Science 133:1702–1703

Denny FB, et al (2008) The Illinois-Kentucky Fluorite District, Hicks Dome, and Garden of the Gods in southeastern Illinois and northwestern Kentucky. In: Maria AH, Counts RC (eds) From the Cincinnati Arch to the Illinois Basin: Geological Field Excursions along the Ohio River Valley. Geological Society of America, pp 11–24

Giggenbach WF (1992) Isotopic shifts in waters from geothermal and volcanic systems along convergent plate boundaries and their origin. Earth and Planetary Science Letters 113:495–510

Kendall C, Coplen TB (2001) Distribution of oxygen-18 and deuterium in river waters across the United States. Hydrological Processes 15:1363–1393

Labotka DM, et al (2015) Isotopic and geochemical characterization of fossil brines of the Cambrian Mt. Simon Sandstone and Ironton–Galesville Formation from the Illinois Basin, USA. Geochimica et Cosmochimica Acta 165:342–360

Moorehead A (2013) Igneous intrusions at Hicks Dome, southern Illinois, and their relationship to fluorine-base metal-rare earth element mineralization. M.Sc. Thesis, Southern Illinois University

O'Neil JR, Taylor Jr. HP (1969) Oxygen isotope equilibrium between muscovite and water. Journal of Geophysical Research (1896-1977) 74:6012–6022

O'Neil JR, Kharaka YK (1976) Hydrogen and oxygen isotope exchange reactions between clay minerals and water. Geochimica et Cosmochimica Acta 40:241–246

Pinckney DM, Rye RO (1972) Variation of O^{18}/O^{16}, C^{13}/C^{12}, texture, and mineralogy in altered limestone in the Hill Mine, Cave-in-District, Illinois. Economic Geology 67:1–18

Plumlee GS, Goldhaber MB, Rowan EL (1995) The potential role of magmatic gases in the genesis of Illinois-Kentucky fluorspar deposits; implications from chemical reaction path modeling. Economic Geology 90:999–1011

Richardson CK, Rye RO, Wasserman MD (1988) The chemical and thermal evolution of the fluids in the Cave-in-Rock fluorspar district, Illinois; stable isotope systematics at the Deardorff Mine. Economic Geology 83:765–783

Sharp ZD, Atudorei V, Durakiewicz T (2001) A rapid method for determination of hydrogen and oxygen isotope ratios from water and hydrous minerals. Chemical Geology 178:197–210

Suzuoki T, Epstein S (1976) Hydrogen isotope fractionation between OH-bearing minerals and water. Geochimica et Cosmochimica Acta 40:1229–1240

Taylor Jr. HP, Sheppard SMF (1986) Igneous rocks: I. Processes of isotopic fractionation ad isotope systematics. In: Valley JW, Taylor Jr. HP, O'Neil JR (eds) Stable Isotopes in High Temperature Geological Processes. Mineralogical Society of America, pp 227–271

U.S. Geological Survey (2022) 2022 Final List of Critical Minerals [notice], Federal Register 87:10381–10382

Zheng Y-F (1993) Calculation of oxygen isotope fractionation in hydroxyl-bearing silicates. Earth and Planetary Science Letters 120:247–263

Iron-Ti oxide and apatite mineralisation associated with alkaline monzonitic rocks: An example from the Kodal deposit, Permian Oslo Rift, Norway

Ana Carolina R. Miranda[1], Nolwenn Coint[1], Sarah Dare[2] and Eduardo T. Mansur[1]
[1]Geological Survey of Norway, Trondheim, Norway
[2]Department of Applied Sciences, Université du Québec à Chicoutimi, Chicoutimi, Canada

Abstract. Iron-Ti oxide and apatite enriched rocks are typically associated with anorthosite–mangerite–charnockite–granite (AMCG) and layered intrusions in magmatic systems or related to iron oxide apatite (IOA) deposits, in hydrothermal systems. The origin of these non-cotectic rocks in magmatic systems has been widely debated and several petrogenetic models have been proposed. The Kodal deposit, located in the Permian Oslo rift, South Norway, is the largest occurrence of Fe-Ti oxide and apatite mineralisation hosted within alkaline monzonitic rock, differing from known occurrences hosted within AMCG suites and mafic layered intrusions. The Fe-Ti oxide and apatite mineralisation consists of disseminated and massive ore, which are mainly composed of variable amounts of titanomagnetite, apatite and augite and minor amphibole and biotite. We have systematically sampled four representative drill cores across the Kodal deposit. Further investigation of the concentration of the trace elements in titanomagnetite and apatite in the host rock, disseminated and massive ores will be performed by LA-ICP-MS. This will allow us to assess which petrogenetic processes, such as liquid-liquid immiscibility, fractional crystallization or mineral accumulation, contributed to the formation of Fe-Ti oxide and apatite mineralisation at Kodal.

1 Introduction

The Fe-Ti oxide and apatite-rich rocks (i.e. nelsonites) of magmatic origin are commonly associated with mafic and intermediate intrusive complexes related to anorthosite–mangerite–charnockite–granite (AMCG) and layered intrusions (Dymek and Owens 2001; Charlier et al. 2008; Coint et al. 2020). In hydrothermal systems, these are commonly related to iron oxide apatite deposits (IOA). Nevertheless, the origin of these non-cotectic rocks has been widely debated and petrogenetic models evoking fractional crystallization, liquid-liquid immiscibility, mineral accumulation and residual melts concentrated by filter pressing have been proposed as alternatives to explain their origin (Philpotts 1967; Emslie 1975).

Discovered in the late eighteen hundreds, the Kodal deposit is one of the largest Fe-Ti oxide and apatite deposits in Norway (Figure 1). Different from known occurrences hosted within AMCG suites and mafic layered intrusions, the Fe-Ti oxide and apatite mineralisation at Kodal is hosted within alkaline monzonite. Three distinct models have been proposed to explain the genesis of the Kodal deposit: (i) silicate-liquid immiscibility leading to the separation of an Fe-rich melt (Bergstøl 1972; Kragh

and Jensen 1991); (ii) fractional crystallization and physical accumulation of apatite and Fe-Ti-oxides from a monzonitic magma (Peterson 1978); and (iii) apatite and Fe-Ti oxide crystallization at depth followed by upward transport, accompanied by mineral sorting, to shallow crustal levels (Andersen and Seiersten 1994).
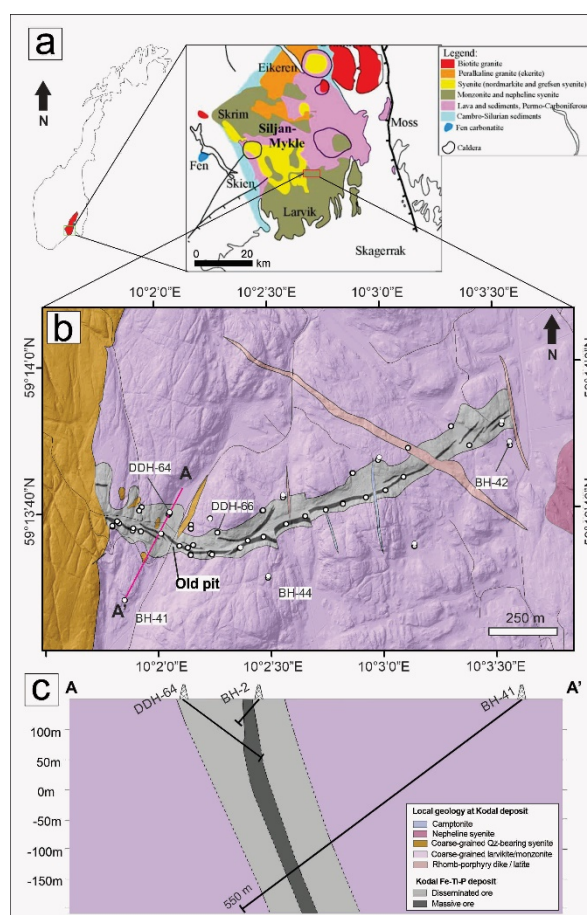
Figure 1. a. Simplified regional geological map of the southern part of Oslo rift showing the location of Kodal Fe-Ti-P deposit; b. Geological map showing the Kodal deposit. The white dots represent the location of drill cores; c. Profile containing three drillcores showing the shape and orientation of the ore body.

Considering that the genesis of Kodal deposit is poorly understood and that the Fe-Ti-P mineralisation is hosted in monzonitic rocks, the Kodal deposit offers the opportunity to understand a so far unique Fe-Ti-P mineralisation hosted in evolved, alkaline magmatic rocks.

In this work, we report preliminary results of fieldwork, and petrographic description of the host rock and Fe-Ti-P ores of the Kodal deposit. Further investigation of trace elements in titanomagnetite and apatite will be performed to test the different hypotheses for the formation of the Kodal deposit.

2 Geological setting of the Kodal Fe-Ti-P deposit

The Kodal deposit is located in the Permian Oslo Rift at the southern part of Norway (Figure 1). It represents the largest occurrence of Fe-Ti-P mineralisation in the Larvik Plutonic Complex (LPC), with a total indicated resource of 14.6 Mt at 5.18% P_2O_5 and 24.12% Fe (Kodal Minerals PLC 2014). The LPC comprises a slightly- to under-saturated, alkaline monzonite (regionally referred to as larvikite), syenite and nepheline-syenite (regionally referred to as lardalite), formed during the Permian rifting (Petersen 1978). These intrusions form several rings, which suggests sequential shifting of centres of magmatic activity towards the west, with the nepheline-syenite being the youngest phase (Petersen 1978; Rämö et al., 2022). The positioning of the Kodal deposit within the LPC is not well constrained, but it is possible that the deposit is associated with the latest magmatic pulses in the region.

The Kodal deposit is poorly exposed, except for an old mining pit area, where massive nelsonites can be observed (Figures 1 and 2a). The Fe-Ti-P orebody consists of an approximately 2 km long, and 100 meters thick, tabular, E-W trending orebody, steeply dipping (70-80 degrees) towards the south (Figure 1). The ore consists of variable amounts of titanomagnetite, apatite and augite, with minor amphibole and biotite. It can be massive or disseminated where it constitutes up to 40% of the total volume of the rock (Figure 2). The massive ore varies from a few centimetre intervals that occur as pockets within the monzonite, displaying sharp contacts, to zones with approximately 2 metres of thickness, normally surrounded by disseminated intervals (Figures 1 and 2).

Around 40 cores were drilled in the Kodal deposit in the early 1980's, which allows us to precisely constrain the geometry of the ore body and detailed sampling of different portions of the mineralisation. Whole-rock geochemical analyses for the cores yield in average 1.33 wt.% P_2O_5, 12.3 wt.% Fe_2O_3(T) and 2.4 wt.% TiO_2 for the host monzonite, 2.7 wt.% P, 19.1 wt.% Fe_2O_3(T) and 4.18 wt.% TiO_2 for the disseminated ore, and 7.3 wt.% P_2O_5, 44.7 wt.% Fe_2O_3(T) and 8.63 wt.% TiO_2 for the massive ore. Thus, the limit between the monzonite and the disseminated ore (Figure 1) is mostly based on Fe_2O_3(T), TiO_2 and P_2O_5 concentrations, but local variations are common and the profile showed in the Figure 1c is just a schematic simplification of the ore types.

The relationship between the host rocks and the different ore types is variable, but magmatic flow textures are commonly observed (Figure 2). In these cases, coarse-grained feldspar crystals from the host monzonite display a parallel alignment and accompany domains with massive Fe-Ti-P ore (Figure 2b). Moreover, although a gradual transition from host rock to disseminated and to massive ore has been observed, a sharp contact between massive ore and the host rock is also common (Figure 2c). Overall, the textures suggest that the host monzonite and the Fe-Ti-P-rich domains co-existed, and were eventually mobilized together, prior to complete crystallization.

3 Methods

We have systematically described and sampled four representative drill cores across the deposit (Figure 1). Over 100 samples have been collected, and 44 thin sections were prepared and characterized under reflected and transmitted light.

The concentration of trace element in Fe-oxides (Ti-magnetite and ilmenite) and apatite in the host rock, disseminated and massive ores will be obtained by LA-ICP-MS, at the Geological Survey of Norway.

4 Preliminary results

The host monzonite is predominantly composed of dark grey coarse-grained feldspar crystals (ternary feldspar), associated with accumulations of interstitial domains of fine-grained mafic minerals (Figure 3a). These interstitial domains (approximately <10% of the rock) comprise titanomagnetite, with ilmenite lamellae exsolutions, apatite and augite (Figures 3a and 4a). Apatite crystals occur as inclusions in magnetite and augite crystals, but also as euhedral crystals with well-defined contacts with other phases. Amphibole and biotite are observed as a product of augite alteration, normally concentrated in fractures and along augite rims (Figure 4a). Commonly, centimetre-scale agglomerates of titanomagnetite are surrounded by a thin rim of titanite crystals at the contact with surrounding silicates (Figure 4a). In weathered examples, the monzonite displays a pale/whitish colour as a result of the alteration of large feldspar crystals (Figure 2a). The degree of such alteration is variable, but can be pervasive, characterizing a complete change of feldspar colour, or partial, where only the rims of feldspar crystals are transformed to a very-fine grained aggregate of sericite. In cases where pervasive alteration is observed, the magmatic texture of the rock is still preserved, and the only remarkable feature is the change in the rock colour (Figure 2b).
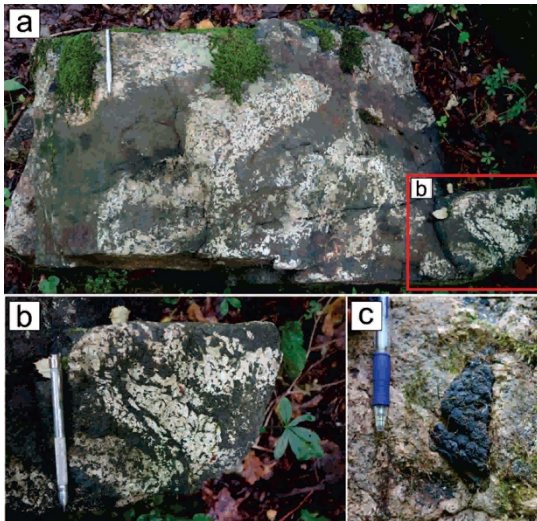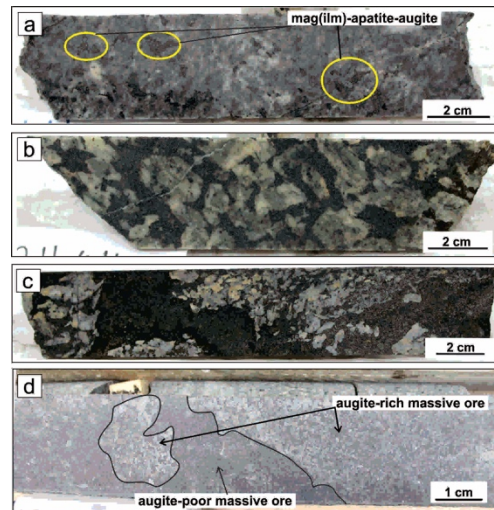
Figure 2. a. Sample close to the old excavation pit at Kodal deposit. The host monzonite displays a magmatic flow texture defined by the alignment of rhomb-shaped feldspar phenocrysts and centimetric domains of massive Fe-Ti-P ore; b. Monzonite with massive Fe-Ti-P ore displaying folded magmatic foliation. The white colour of coarse-grained euhedral feldspar crystals is a result of surface weathering; c. Outcrop near the old excavation pit displaying a centimetric massive oxide-apatite bleb within the host monzonite. Note the sharp contact between the massive ore and the host rock.


Figure 3. Representative facies of the Kodal Fe-Ti-P deposit. a. Monzonite hosting euhedral feldspar crystals surrounded by interstitial domains of mafic minerals (i.e., augite, titanomagnetite, apatite and minor ilmenite); b. Net-textured Fe-Ti-P ore (dark) surrounding grey-coloured, partially altered, feldspar crystals; c. Contact between the net-textured and massive Fe-Ti-P ores. Note the sharp contact between the two; d. Massive Fe-Ti-P ore with augite-rich and augite-poor domains. Note the sharp contact between both facies, and the occurrence of irregular blebs of the augite-rich ore within augite-poor domains.

Disseminated ore is more abundant relative to massive ore within the Kodal deposit (Figure 1). Iron-Ti oxide (most commonly titanomagnetite and minor ilmenite), apatite and augite accumulations form a more or less connected interstitial network around alkali feldspar phenocrysts. Locally, a greater proportion of the interstitial mafic minerals relative to feldspar led to the development of a net-textured ore (Figures 3b-c). In these cases, the mafic minerals define an interstitial continuum within large feldspar crystals and their volume can reach up to 40%.

The massive ore is composed mainly of apatite and titanomagnetite with variable amounts of augite. It can be divided into augite-poor and augite-rich massive ore (Figure 3d). In the augite-rich domains, the augite crystals are medium- to fine-grained and commonly display amphibole and biotite alteration along the edges (Figures 4a and 4b). Augite-poor domains comprise predominantly titanomagnetite and apatite, with minor titanite. Apatite occurs included within larger magnetite crystals or displaying sharp contact with smaller crystals. The proportion of apatite varies, but is commonly greater than 30% of the rock volume.

The transition between disseminated and massive ore domains is variable and can be given by a progressive increase of apatite and magnetite, but most frequently is marked by a sharp contact. Round-shaped pockets of massive ore of few tens of centimetres are also commonly found embedded within the disseminated ore, but less frequently in direct contact with the host monzonite (Figure 2c).

5 Concluding remarks and next steps

A remarkable feature of the Kodal deposit is the presence of magmatic flow textures in the ore (Figure 2c), defined by the alignment of alkali feldspar. Although our preliminary results do not allow us yet to constrain the ore forming processes that led to the formation of the deposit, the textures are indicative that magmatic flow played a role in the segregation of the Fe-Ti-P ore minerals. This is important as a process leading to the non-cotectic accumulation of augite, apatite and magnetite is required in order to explain the origin of the Kodal deposit.

To improve our understanding of the formation of the Kodal deposit, we will systematically investigate the trace-element composition of magnetite and apatite in different portions and facies of the deposit. Recent contributions have shown that these results can be used to unveil processes, such as accumulation during fractional crystallization or silicate-liquid immiscibility (Dare et al. 2014; Arguin et al. 2018; Coint et al. 2020; Kieffer et al., 2023). Moreover, although studies assessing the composition of apatite and Fe-oxides in Fe-Ti-P-rich rocks formed at different geological settings has gained more attention in recent years, this is not yet the case for alkaline systems. As such, the Kodal deposit offers the opportunity to unveil the chemistry of these minerals in an Fe-Ti-P deposits formed at as part of alkaline system, which, to the best of our knowledge has not yet been assessed elsewhere.
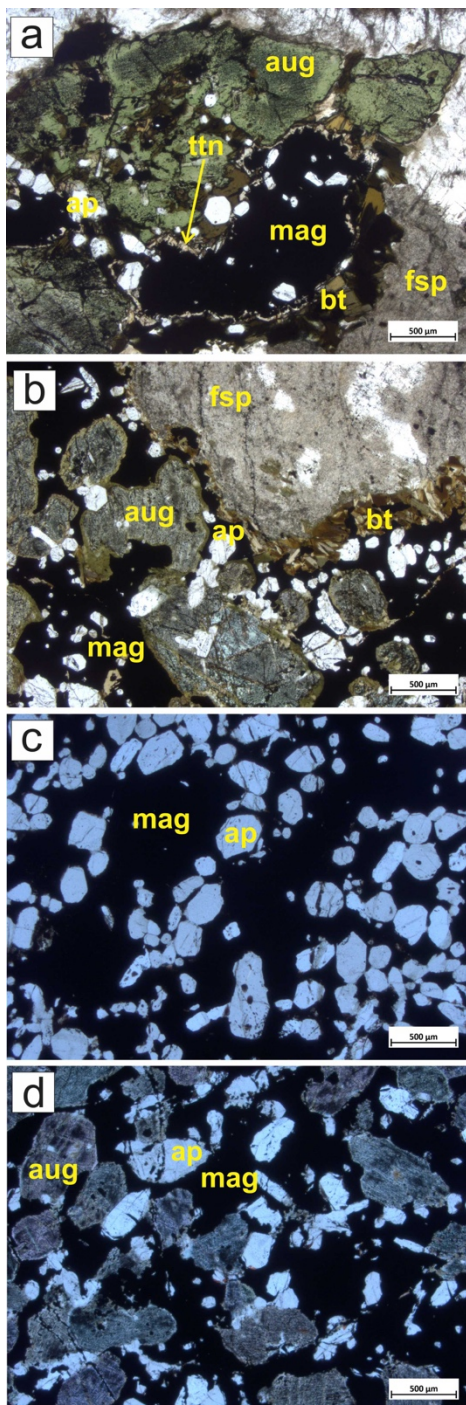
Figure 4. Transmitted light photomicrographs of the monzonitic host-rock of the Kodal deposit and different Fe-Ti-P ore types. a. Local accumulation of titanomagnetite and apatite within augite crystals in the monzonite. Note the occurrence of a thin rim of titanite at the contact between magnetite and surrounding silicates; b. Net-textured ore with titanomagnetite and apatite domains surrounding a coarse-grained. Note the partial alteration of the feldspar crystal and the biotite-rich contact between the feldspar and magnetite; c. Augite-poor massive ore comprising abundant euhedral apatite crystals both included within and at contact with magnetite; d. Augite-rich massive ore with partial alteration of the augite crystals along fractures and rims. Abbreviations: aug: augite; ap: apatite; bt: biotite; fsp: feldspar. ttn: titanite; mag: magnetite.

References

Andersen T and Seiersten M (1994) Deep cumulates in a shallow intrusion: Origin and crystallization history of a pyroxenite (jacupirangite s.l.) body in the Larvik Pluton, Oslo Region, South Norway. N. Jb. Miner. Mh., H. 6,255 - 274

Arguin J-P, Pagé P, Barnes S-J, Girard R, Duran C (2018) An Integrated Model for Ilmenite, Al-Spinel, and Corundum Exsolutions in Titanomagnetite from Oxide-Rich Layers of the Lac Doré Complex (Québec, Canada). *Minerals* 8(11):476. https://doi.org/10.3390/min8110476

Bergstøl S (1972) The Jacupirangite at Kodal, Vesffold, Norway. (A potential Magnetite, ilmenite and apatite ore). Mineral. Deposita 7:283-246

Charlier B, Sakoma E, Sauvé M, Stanaway K, Auwera JV, Duchesne JC (2008) The Grader layered intrusion (Havre-Saint-Pierre Anorthosite, Quebec) and genesis of nelsonite and other Fe–Ti–P ores. Lithos 101:359-378, https://doi.org/10.1016/j.lithos.2007.08.004.

Coint N, Keiding JK, Ihlen PM (2020) Evidence for Silicate–Liquid Immiscibility in Monzonites and Petrogenesis of Associated Fe–Ti–P-rich rocks: Example from the Raftsund Intrusion, Lofoten, Northern Norway, *Journal of Petrology* 61 (4) egaa045 https://doi.org/10.1093/petrology/egaa045

Dare SAS, Barnes SJ, Beaudoin G, *et al.* (2014) Trace elements in magnetite as petrogenetic indicators. *Miner Deposita* **49**, 785–796 https://doi.org/10.1007/s00126-014-0529-0

Dymek RF, and Owens BE (2001) Petrogenesis of Apatite-Rich Rocks (Nelsonites and Oxide-Apatite Gabbronorites) Associated with Massif Anorthosites. *Economic Geology* 96(4):797–815. doi: https://doi.org/10.2113/gsecongeo.96.4.797

Emslie RF (1975) Major rock units of the Morin Complex, southwestern Quebec: Geological Survey of Canada Paper 74-48, 37p.

Kieffer MA, Dare SA, and Namur O (2023) The use of trace elements in apatite to trace differentiation of a ferrobasaltic melt in the Sept-Iles Intrusive Suite, Quebec, Canada: Implications for provenance discrimination. *Geochimica et Cosmochimica Acta* 342:169-197

Kodal Minerals plc. (2014) *Group Annual Report and Financial Statements for the year ended 31 March 2014.* Kodal Minerals plc, London.

Kragh K and Jensen OA (1991) An immiscible iron-rich liquid in a larvikite magma? GeoSkrifter 38: 32-34

Petersen JS (1978) Structure of the larvikite-lardalite complex, Oslo Region, Norway, and its evolution. Geol. Rundschau 67,330-342.

Philpotts AR (1967) Origin of certain iron-titanium oxide and apatite rocks: Economic Geology, 62:303–315

Rämö OT, Andersen T, and Whitehouse MJ (2022) Timing and Petrogenesis of the Permo-Carboniferous Larvik Plutonic Complex, Oslo Rift, Norway: New Insights from U–Pb, Lu-Hf, and O Isotopes in Zircon. Journal of Petrology, 63(12), egac116

Fengchengite from Sierra La Vasca Complex, Mexico

Maria Grazia Perna[1], Antonio Rodriguez Vega[2], Emma Humpreys-Williams[3], Fabrizio Nestola[4], Biagioni Cristian[5], Gianluigi Rosatelli[1], Francesco Stoppa[1]

[1] Department of Psychological, Health and Territory Sciences, University "Gabriele d'Annunzio" Chieti-Pescara, 66100, Chieti, Italy
[2] Escuela Superior de Ingeniería (ESI) Universidad Autónoma de Coahuila. Boulevard Adolfo López Mateos s/n, Nueva Rosita, San Juan de Sabinas, Coahuila.
[3] The Natural History Museum, London SW7 5BD, UK
[4] Department of Geosciences, Padua University, 35121 Padova, Italy
[5] Department of Earth Sciences, Pisa University, 56126 Pisa, Italy

Abstract. Fengchengite is a member of eudialyte group-minerals, with a general formula $Na_{12}\square_3Ca_6(Fe^{3+},\square)_3Zr_3Si(Si_{25}O_{73})(H_2O)_3(OH)_2$. The cell parameters are a=14.2426 Å, c=30.1889 Å, V=5303.32 Å^3 and the space group is $R\bar{3}m$. The genetic environment is associated with highly evolved peralkaline igneous products. The associated paragenesis consists of alkali feldspars, aegirine, arfvedsonite, apophyllite, calcite and other mineral phases at REE, corresponding to the typical mineralogy of a kakortokite, a variety of agpaitic nepheline syenite displaying cumulate textures and igneous layering. Kakortokite is associated with wollastonite, containing goetzenite, brytholite and pyrite. Fengchengite is a rare mineral with a puzzling structure that is difficult to reconstruct.

1 Introduction

The economic importance and demand for high field strength elements (HFSE) and rare earth elements (REEs) have increased significantly in recent years (e.g. Weng et al. 2015; Goodenough et al. 2017), especially in the last period due to the political crisis. They form the basis for transitioning to a high-tech, green-tech and sustainable industry. This has led to the development and search for new deposits and sources that can lead to the extraction of such products. Alkaline complexes are placed in this perspective, where the close association between carbonatitic and alkaline rocks represents one of the largest reservoirs of REE and HFSE (e.g. Dostal 2017). Rocks from these complexes show an unusual enrichment in these elements and a typical mineralogy composed of REE-bearing rare and complex minerals.

Peralkaline igneous rocks are characterised by a molar ratio (Na+K)/Al >1. Depending on the HFSE-bearing minerals, a distinction is made between miaskitic rocks, in which HFSE are mainly hosted by zircon/baddeleyite and titanite/perovskite, and agpaitic rocks, in which HFSE are hosted by Na-Ca-HFSE complex minerals, in particular eudialyte group minerals (EGMs, hereafter), rinkite group minerals and wöhlerite group minerals (e.g. Marks and Markl 2017).

The EGMs are represented by HFSE-REE-rich Na-Ca-zirconosilicates and represent the index mineral for agpaitic peralkaline systems. The first occurrences were reported from Kangerdluarssuk, Ilìmaussaq, South Greenland (Stromeyer 1819).

The accepted IMA formula (Johnsen et al. 2003a) is as follows:
$\{N(1)_3N(2)_3N(3)_3N(4)_3N(5)_3\}\{[M(1a)_3M(1b)_3]_3M(2)_3M(3)M(4)Z_3[Si_{24}O_{72}]\varnothing_{0-6}\}X(1)X(2)$
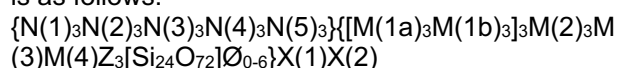
EGMs are currently composed of 30 chemical species (for the empirical and corresponding CNMNC formulae of the IMA-approved members of the eudialyte group, see Mikhailova et al. 2022 and references therein).

This mineral group is known from various occurrences, including the Lovozero alkaline massif, Russia (e.g. Mikhailova et al. 2020), the Ilìmaussaq complex, South Greenland (e.g. Marks et al. 2020), Mont Saint Hilaire, Quebec, Canada (e.g. Johnsen et al. 2003b), Tamazeght, Morocco (e.g. Schilling et al. 2009), Norra Kärr alkaline complex, Southern Sweden (e.g. Sjoqvist et al. 2013) and many others. The minerals typically associated with EGMs in these occurrences are aegirine and arfvedsonite, various Na-Al silicates such as alkali feldspars, nepheline, sodalite, zeolites and various HFSE and LILE-rich minerals such as astrophyllite, lamprophyllite, tugtupite, wohlerite, rosenbuschite and rinkite) (Schilling et al. 2011).

2 Geological Setting

Sierra La Vasca represents a Tertiary magmatic complex with an extension of approximately 100 km^2 and. It consists of two main intrusive bodies of granitic and monzonitic composition, associated with numerous minor intrusive bodies, including dykes and sills, of compositions varying between diorite, andesite, dacite and rhyolite. The area also presents a series of satellite minor complexes characterised by mainly alkaline and carbonatitic magmatism. Generally, the contact between carbonatitic and syenitic bodies is characterised by centimetric bars of wollastonite rocks. The Cretaceous carbonate sequence represents the basement.

3 Methods

Minerals analysis and BSE images were obtained using a Phenom XL SEM hosted at the DATA Laboratory at "G. d'Annunzio" University of Chieti-Pescara.

Eudialyte-group minerals were analysed by a JEOL 8200 Super-probe at Natural History Museum,

London. The accuracy of these analyses in analysing REE is ~1.3%, based on the detection limit. The detection limit is two magnitude orders lower than the hellandite group members' REE concentration.

Trace element concentrations were acquired using an ESI 213 nm Laser Ablation system and Agilent 7700 ICP-MS system at the Natural History Museum, London.

Spectra data reduction was performed using the Thermo Scientific™ OMNIC™ 9.2.0 Spectral Software at Padua University, Padua, Italy. Single-crystal XRD data were collected using a Supernova Rigaku Oxford Diffraction four-circle diffractometer (Rigaku) equipped with a 200K Pilatus Dectris detector (Dectris). The diffractometer was operated with Mo Kα radiation at 50 kV and 0.12 mA X-ray tube conditions.

Powder XRD was carried out using the X-ray diffractometer Bruker D2 Phaser, located at DATA (Chieti, Italy). The acquisition parameters are Cu-Kα (1.540598 Å) radiation generated at 30 kV and 15 mA in an exploratory interval between 3 and 70° 2θ, 0.1 steps, and a scan rate of 0.15°/s. Once the diffractogram was obtained, background subtraction and indexing of peaks with semi-quantitative analysis were performed. Finally, the mineral identification was performed using the software EVA.

3 Petrographic context

EGMs samples comes from a kakortokite, an agpaitic nepheline syenite. Kakortokite has alkali feldspars, aegirine, arfvedsonite and apophyllite as its main minerals (Figure 1). Accessory minerals are represented by other phases of REE minerals, including F-britholite, stillwellite-(Ce), kainosite-(Y) and gittinsite, a typical alteration mineral of the eudialyte group.
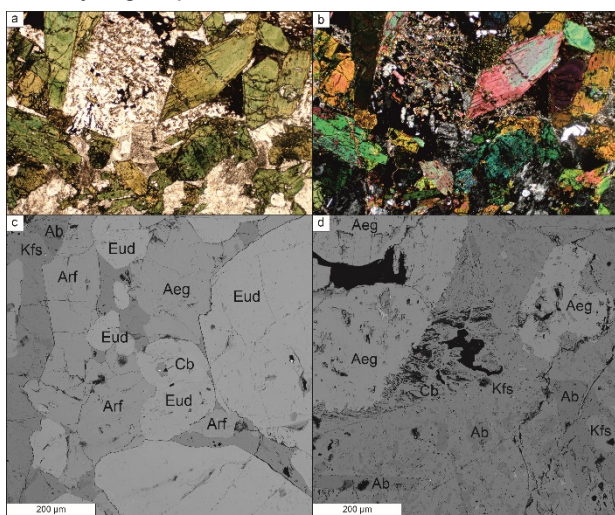
Figure 1. a-b. Plane-polarised (left) and cross-polarised (right) transmitted light images for kakortokite sample; c-d. BSE images of kakortokite sample. Abbreviation: Ab- albite; Kfs- k-feldspar; Eud- eudialyte group minerals; Aeg – aegirine; Arf – arfvedsonite; Cb – carbonate.

4 Crystal structure

The structure of the eudialyte group of minerals is hetero-polyhedral, with three layers alternating along the c-axis. The T-layer is characterised by three- or nine-membered SiO_4 tetrahedra, $[Si_3O_9]^{6-}$ or $[Si_9O_{27}]^{18-}$, respectively; the M-layer is formed by 6-membered rings of $[M(1)_6O_{24}]$ built by shared $M(1)O_6$ octahedra along one edge; and isolated octahedra of ZO_6 form the Z-layer. They alternate in *TMTZ* mode (Rastsvetaeva 2007).

In the complex structure, the SiO_4 rings combined in $[Si_3O_9]^{6-}$ and $[Si_9O_{27}]^{18-}$ form layers perpendicular to [001]. Between two of these, rings of $[M(1)O_6]$ octahedra are connected by polyhedra of $[M(2)O_n]$, forming 2:1 layers. Zr cross-links these layers in octahedral coordination. The final presence of $[NaO_n]$ polyhedra, where Na can have different coordination, implies the filling of the structure. These structures form a trigonal system with space group $R3m$, $R\bar{3}m$ or $R3$. In the case of $R\bar{3}m$, the presence of the centre of symmetry between Si(1) and Si(2) reduces the number of different sites (Johnsen and Grice 1999). Furthermore, the N sites, which are 5 in the case of $R3m$ and $R3$, are reduced to 3, with Na(1) equal to Na(2) and Na(3) equals Na(4). In this case, these N sites are entirely occupied by Na, except in the case of fengchengite, which is characterised by vacancies on the N(3) site (see Mikhailova et al. 2022).

The crystal structure of our eudialyte sample is solved on MoKα radiation and refined for 1929 unique reflections. The space group is trigonal, $R\bar{3}m$ with a=14.2426 Å and c=30.1889 Å, V=5303.32 Å^3.

5 Crystal chemistry

The chemical composition of eudialyte group minerals (in average and in wt.%) is SiO_2 51.2, ZrO_2 11.7, Nb_2O_5 0.3, TiO_2 0.8, Ta_2O_5 0.1, FeO 5.4, MnO 1.0, CaO 11.1, Na_2O 12.9, K_2O 0.2, La_2O_3 0.3, Ce_2O_3 0.9, Pr_2O_3 0.1, Nd_2O_3 0.4, Sm_2O_3 0.1, Gd_2O_3 0.1, Y_2O_3 0.4, HfO_2 0.2, Cl 2.2.

The formula recalculated based on Si+Zr+Ti+Hf+Nb= 29 (following Johnsen and Grice 1999) (in average and in a.p.f.u.) is Si 25.7, Zr 2.9, Nb 0.1, Ti 0.3, Fe 2.3, Mn 0.4, Ca 6.0, Na 12.5, K 0.1, La 0.1, Ce 0.2, Nd 0.1, Y 0.1, Cl 1.9.

6 Conclusion

Classifying minerals of the eudialyte group is a complex process which requires a thorough overview of the crystal structure and chemical composition.

Regarding the crystal structure, following Rastsvetaeva and Chukanov (2012), our sample turns out to be "12-layer eudialyte" being a=14.2426 Å and c=30.1889 Å, M(1)-disordered with spatial group $R\bar{3}m$ and, based on centring nine-membered Si, O rings by the additional Si-tetrahedra (T), M-octahedra (M) or vacancies (□) or combination of these, our sample falls into the T+T variant.

In terms of chemical composition, the classification was performed following Mikhailova et al. (2022). Our sample shows Zr> 2.25 belonging to the Zirconium eudialytes. The content of Ca is > 4.5 belonging to the subgroup of the Ca-rich Zirconium eudialytes. From the structural analysis, it belongs to the T+T variant with Si> 25.5, Nb < 0.5 and W < 0.5. Based on the content of Mn and Fe and their occupancy in the M(2) site, with $4.5 \geq$ $^{M(2)}$Mn + $^{M(2)}$Fe > 1.5; $^{M(2)}$Fe > $^{M(2)}$Mn; $Fe^{3+} > Fe^{2+}$ our sample falls into the fengchengite group. This is in agreement with the structure as fengchengite is the only 12-layer end-member with space group $R\overline{3}m$.

The final formula is $^{N}\{[Na_{3.00}Na_{3.00}]_{\Sigma 6.00}(Na_{5.55}K_{0.13}$ $Sr_{0.01}Ca_{0.31})_{\Sigma 6.00}(\square_{2.70}Ca_{0.08}Mn^{2+}_{0.22})_{\Sigma 3.00}\}_{\Sigma 15.00}$ $^{M(1)}(Ca_{5.61}La_{0.05}Ce_{0.13}Pr_{0.01}Nd_{0.06}Sm_{0.01}Gd_{0.01}Dy_{0.01}$ $Er_{0.01}Yb_{0.01}Y_{0.10})_{\Sigma 6.00}$$^{M(2)}(Fe^{3+}_{2.52}Mn^{2+}_{0.21}Ti_{0.26}Ta_{0.01})_{\Sigma 3.00}$ $^{Z}(Zr_{2.87}Nb_{0.08}Ti_{0.03}Hf_{0.03})_{\Sigma 3.00}$ $^{M(3)}Si_{0.73}$ $^{M(4)}Si_{25}$ O_{73} $^{X(1)}(H_2O)_3$ $^{X(2)}(Cl_{1.89}OH_{0.11})_{\Sigma 2.00}$.

Acknowledgements

References

Dostal J (2017) Rare Earth Element deposits of alkaline igneous rocks. Resources 6(3):34. https://doi.org/10.3390/resources6030034

Goodenough KM, Wall F, Merriman D (2017) The Rare Earth Elements: demand, global resources, and challenges for resourcing future generations. Nat Resour Res 27:201-216. https://doi.org/10.1007/s11053-017-9336-5 https://doi.org/10.1134/S1075701512070069

Johnsen O, Grice JD (1999) The crystal chemistry of the eudialyte group. Canad Miner 37: 865–891.

Johnsen O, Ferraris G, Gault RA, Grice JD, Kampf AR, Pekov, IV (2003a) The nomenclature of eudialyte-group minerals. Canad Mineral 41(3):785-794. https://doi.org/10.2113/gscanmin.41.3.785

Johnsen O, Grice JD, Gault RA (2003b) Ferrokentbrooksite, a new member of the eudialyte group from Mont Saint-Hilaire, Quebec, Canada. Canad Mineral 41(1):55-60. https://doi.org/10.2113/gscanmin.41.1.55

Marks MAW, Eggenkamp HGM, Atanasova P, Mundel F, Kümmel S, Hagen M, Wenzel T, Markl G (2020) Review on the compositional variation of Eudialyte-group minerals in the Ilímaussaq Complex (South Greenland). Minerals 10(11):1011. https://doi.org/10.3390/min10111011

Marks MAW, Markl G (2017) A global review on agpaitic rocks. Earth Sci Rev 173:229-258. https://doi.org/10.1016/j.earscirev.2017.06.002

Mikhailova JA, Pakhomovsky YA, Panikorovskii TL, Bazai AV, Yakovenchuk VN (2020) Eudialyte group minerals from the Lovozero Alkaline Massif, Russia: occurrence, chemical composition, and petrogenetic significance. Minerals 10(12):1070. https://doi.org/10.3390/min10121070

Mikhailova JA, Stepenshchikov DG, Kalashnikov AO, Aksenov SM (2022) Who is who in the eudialyte group: a new algorithm for the express allocation of a mineral name based on the chemical composition. Minerals 12(2):224. https://doi.org/10.3390/min12020224

Rastsvetaeva RK (2007) Structural mineralogy of the eudialyte group: a review. Crystallogr Rep 52: 47-64.

Rastsvetaeva RK, Chukanov NV (2012) Classification of eudialyte-group minerals. Geol Ore Depos 54:487-497.

Schilling J, Marks MAW, Wenzel T, Markl G (2009) Reconstruction of magmatic to subsolidus processes in agpaitic system using eudialyte textures and composition: a case study form Tamazeght, Morocco. Canad Mineral 47(2):351-365. https://doi.org/10.3749/canmin.47.2.351

Schilling J, Wu F-Y, McCammon C, Wenzel T, Marks MAW, Pfaff K, Jacob DE, Markl G (2011) The compositional variability of eudialyte-group minerals. Mineral Mag 75(1):87-115. https://doi.org/10.1180/minmag.2011.075.1.87

Sjöqvist ASL, Cornell DH, Andersen T, Erambert M, Ek M, Leijd M (2013) Three Compositional Varieties of Rare-Earth Element Ore: Eudialyte-Group Minerals from the Norra Kärr Alkaline Complex, Southern Sweden. Minerals 3(1):94-120. https://doi.org/10.3390/min3010094

Stromeyer F (1819) Analyse einiger von dem Prof. von Giesecke in Grönland entdeckten Fossilien: Gieseckit, Saphirin, Apophyllit, Dichroit, Arragonit und Eudialit. Ann Phys 63:372–381 (in German).

Weng Z, Jowitt SM, Mudd GM, Haque N (2015) A detailed assessment of global Rare Earth Element Resources: opportunities and challenges. Econ Geol 110(8):1925-1952. https://doi.org/10.2113/econgeo.110.8.1925

The Mount Weld rare earth element deposit, Western Australia: a carbonatite-derived laterite

Philip L. Verplanck[1], Heather A. Lowers[1], Adam R. Boehlke[1], Jay M. Thompson[1], Ganesh Bhat[2], Cameron Mercer[1]
[1]US Geological Survey, Denver, Colorado, USA
[2]Lynas Rare Earths Ltd., Laverton, Australia

Abstract. Carbonatite-hosted rare earth element (REE) deposits are the primary source of the world's light REEs and have the potential to be a source of heavy REEs. The Mount Weld REE deposit in Western Australia is hosted in a lateritic sequence that reflects supergene enrichment of the underlying carbonatite complex. Similar to other carbonatite-related ore deposits, ore from Mount Weld displays extreme light REE (LREE) enrichment (La up to 4 wt. %), but in contrast also contains substantially higher concentrations of heavy REEs (HREEs). REE enrichment in the laterite is controlled by the breakdown of primary minerals, the release and transport of REEs, and the formation of secondary minerals. Secondary REE-bearing phosphate minerals are the primary REE-host phases in the laterite ore with monazite as the dominant phase; other REE-bearing phases include rhabdophane, cerianite, churchite, florencite, and crandallite subgroup minerals. Profiles through the laterite show that in the REE-rich zone, apatite and primary calcite have broken down, and dolomite decreases by approximately 60-100%, such that the loss of Ca and Mg, as well as Si and K, leads to a relative increase in the REEs. Sequestering of REEs in secondary mineral phases formed by groundwater further enhances the REE concentration.

1 Introduction

With the increasing reliance on high technology and green energy products, demand for critical metals has become an important driver in economic geology. The REEs are family of elements that have been defined as critical on most lists because of their unique magnetic and optical properties and their geographical-limited supply locations. Carbonatite-hosted REE deposits are the primary source of the world's LREEs and have the potential to be a source of HREEs. Carbonatites are defined by the International Union of Geological Sciences (IUGS) as igneous rocks composed of greater than 50 volume percent primary carbonate minerals, primarily calcite and/or dolomite, and containing less than 20 wt.% SiO_2 (Le Maître 2002). The Mount Weld REE deposit (Figure 1) in Western Australia is hosted in a lateritic sequence above an underlying carbonatite. It is one of four giant, active REE mines associated with carbonatites, the largest REE producer outside of China, and the only one of the four that is laterite hosted. Lynas Rare Earths Ltd. (2022) reported a total mineral resource (measured, indicated, and inferred) of 54.7 million tonnes with 5.3 percent TREO (total rare earth oxide).

The Mount Weld carbonatite occurs within Eastern Goldfields province of the Yilgarn craton, near Laverton, Western Australia. The laterite is covered by 20 to 40 m of lacustrine and alluvial sedimentary rocks, so there is no surface expression of the mineralization. The deposit was discovered by drilling a large, circular magnetic anomaly identified in a 1966 regional airborne geophysical survey undertaken by the Australian Bureau of Mineral Resources. Magnetite from the carbonatite was dated at 2025 ± 10 Ma by the Re-Os method (Graham et al. 2004), but the age of laterization is poorly constrained. Because of active mining and extensive exploration drilling, this is an ideal setting to evaluate REE enrichment associated with lateritically-weathered carbonatites.

Figure 1. Photograph of the Mount Weld mine with the active pit in the foreground, October 2018.

2 Methodology

This study is based on samples from drill cores and from the active pit. Mineralogical characteristics were determined through petrographic studies, scanning electron microscopy (SEM), and X-ray diffraction (XRD). Mineral chemistry on selected samples was determined by Laser Ablation-Inductively Coupled Plasma-Mass Spectrometry (LA-ICP-MS). Major and trace element whole-rock chemistry was determined by wavelength dispersive X-ray fluorescence spectrometry (WDXRF), inductively coupled plasma-optical emission spectroscopy (ICP-OES), and inductively coupled plasma mass spectroscopy (ICP-MS).

3 Results

3.1 The Carbonatite

The Mount Weld carbonatite is approximately 4 kilometers in diameter and is buried under approximately 20-40 meters of surficial sediment and up to 120 meters of weathered material.

Carbonatite samples from older drill core are either calcite- or dolomite-rich, with minor minerals including apatite, magnetite, olivine, biotite, pyrite, monazite, and pyrochlore (Figure 2). Carbonatite samples from core from recent drilling at the base of the active pit are primarily ankerite carbonatite and contain REE fluorcarbonate minerals, bastnäsite and parasite, as well as apatite and monazite. Chondrite-normalized REE diagrams of the Mount Weld carbonatite are LREE enriched, and samples with REE fluorcarbonate minerals are more LREE enriched and have a steeper negative slope (Figure 3). The neodymium isotopic composition (epsilon neodymium calculated at 2025 Ma of 0.7) and strontium isotopic composition ($^{87}Sr/^{86}Sr$ calculated at 2025 Ma of 0.70197) are consistent with the carbonatite being derived from a mantle source (Verplanck et al. 2016).
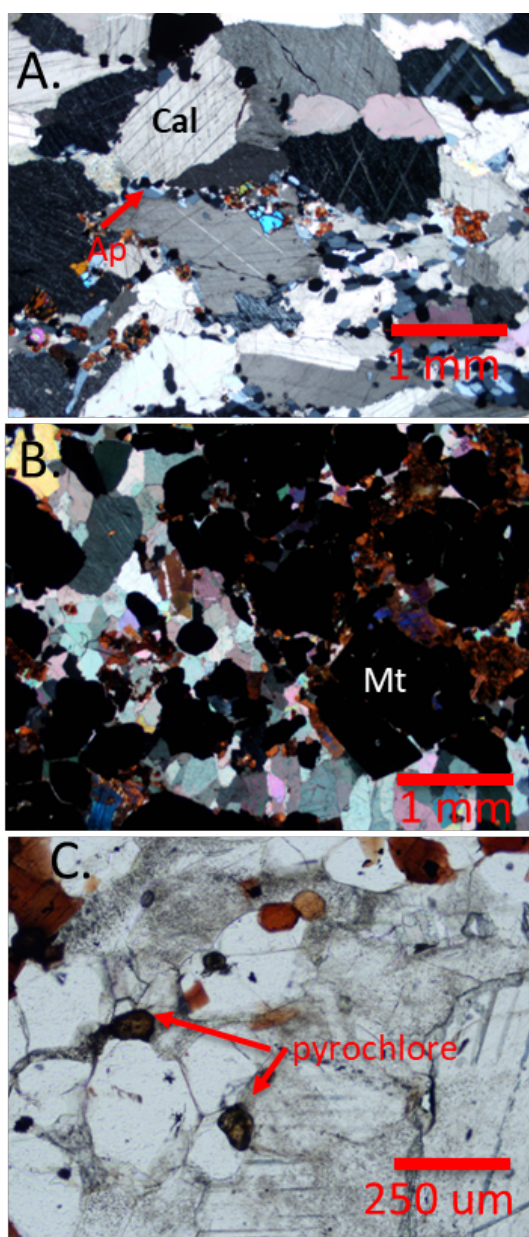
Figure 2. Plane- and cross-polarized light photomicrographs of the Mount Weld carbonatite. a. Calcite (Cal) carbonatite with apatite (Ap); b. Calcite

carbonatite with magnetite (Mt); c. Calcite carbonatite with pyrochlore.
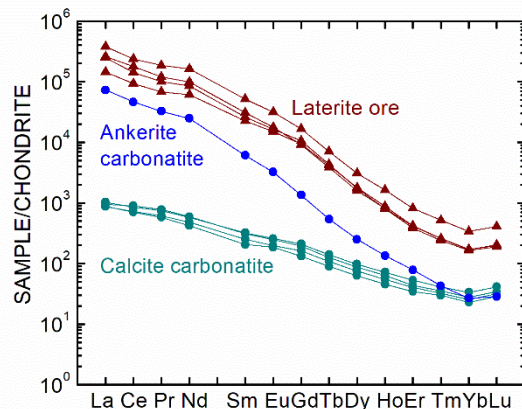
Figure 3. Chondrite-normalized rare earth element diagram displaying the Mount Weld calcite carbonatite, mineralized ankerite carbonatite, and laterite ore. Ankerite carbonatite data from Zhukova et al. 2021. Chondrite values from Anders and Ebihara (1982).
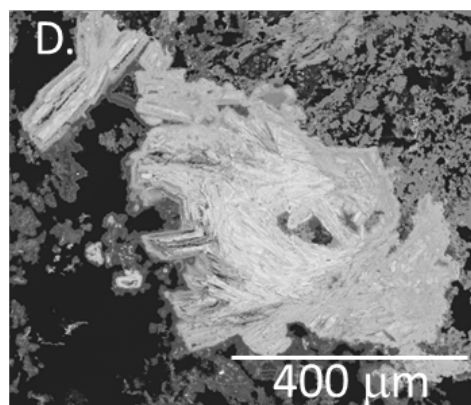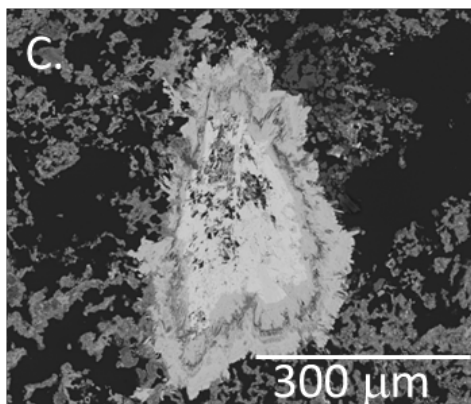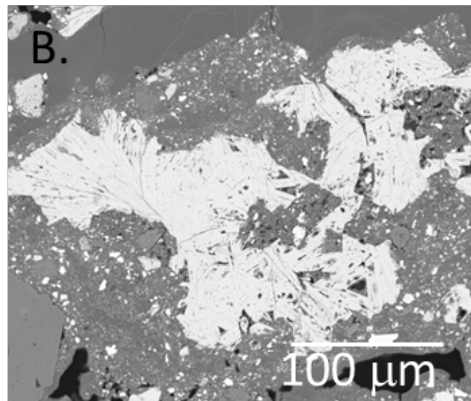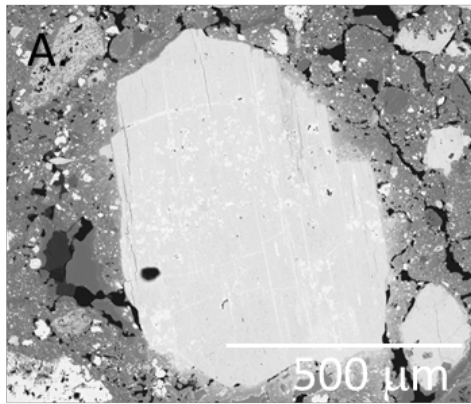
3.1 The Laterite

The laterite sequence, up to approximately 90 m thick, lies above a residual zone that overlays the carbonatite (Figure 4). Overall, the composition of the laterite samples is variable, most samples are iron rich with goethite, the dominant mineral phase. Other minerals include hematite, calcite, dolomite, apatite, hollandite, kaolinite, nacrite, illite, maghemite, montmorillonite, magnetite, pyrochlore, ilmenite, and rutile, and traces of quartz, barite, anatase, cryptomelane, and vermiculite. Calcite and barite appear to be secondary phases while dolomite, magnetite, and pyrochlore are residual phases from the carbonatite. The transition to the underlying carbonatite is termed the "residual zone" and is composed of apatite, magnetite, pyrochlore, and dolomite with secondary goethite, kaolinite, and hematite.

Figure 4. Photograph of an active face near the base of pit at the Mount Weld mine.

The REE mineralogy in the laterite is variable and complex (Figure 5). Within the active pit, medium-grained primary monazite is observed.

Figure 5. Backscatter electron images of REE phases in the laterite. a. Residual grain of primary monazite; b. LREE phase (rhabdophane); c. Zoned churchite; d. Complex phase relationships with intergrown LREE phases.

Secondary phosphate minerals include monazite, rhabdophane [$Ce(PO_4) \cdot 0.6H_2O$], crandallite subgroup minerals (goyazite [$(Sr,REE)Al_3(PO_4)(PO_3OH)(OH)_6$] and gorceixite [$(Ba,REE)Al_3(PO_4)(PO_3OH)(OH)_6$], florencite [$REEAl_3(PO_4)_2(OH)_6$], and churchite [$Y(PO_4) \cdot 2H_2O$]. Cerianite [$CeO_2$] are also observed. Mineral textures are complex displaying variable zoning and overprinting (Figure 5).

The chondrite-normalized REE patterns of samples from the laterite display LREE enrichment but have a range in HREE concentrations (Figure 3 and 6). Compared to the REE patterns of the underlying carbonatite, the ore laterite displays LREE enrichment and substantial HREE enrichment. The LREEs are moderately enriched compared to the ankerite carbonatite, and more substantially enriched compared to the calcite carbonatite (Figure 3). The chondrite-normalized REE patterns for laterite samples from drill core display a range in concentrations, range in slope, and variable sizes of cerium anomalies (Figure 6). These patterns reflect the variability in laterite mineralogy. Samples with more HREEs tend to contain greater proportions of churchite. Relative cerium enrichment or depletion is controlled by redox conditions, thus variations in the nature of the Ce anomalies reflect changing redox conditions during laterite evolution.
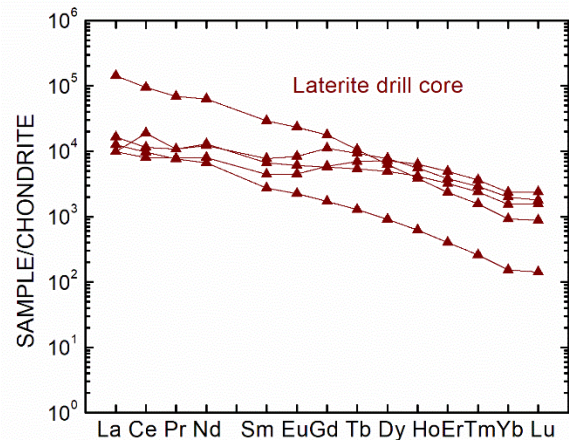
Figure 6. Chondrite-normalized rare earth element diagram displaying laterite samples collected from drill core. Chondrite values from Anders and Ebihara (1982).

4 Discussion

Lateritic weathering is an important process in ore deposit formation. The breakdown of primary minerals and the sequestration of elements in secondary phases may lead to economic enrichments. Carbonatites are characterized by minerals which are susceptible to chemical weathering and by REE concentrations that are enriched compared to most igneous rocks. Chemical weathering of the Mount Weld carbonatite caused the breakdown of minerals including calcite, dolomite, olivine, biotite, magnetite, pyrite, apatite, and monazite. Mass loss by mineral breakdown and elements mobilized in groundwater enhanced the

relative concentration of less mobile elements. Additionally, some elements are sequestered in secondary phases, further enriching the laterite.

In the Mount Weld laterite, primary calcite, olivine, biotite, magnetite, and pyrite are absent. Breakdown of these phases released Ca, Fe, Mg, Si, Al, K, and S. Compared to the carbonatite, dolomite in the laterite decreased by approximately 60-100%, leading to additional release of Ca and Mg. The breakdown of pyrite may have led to isolated zones of acidic conditions which further enhanced chemical weathering. In the carbonatite, the REEs were likely hosted by apatite, monazite, calcite, and dolomite. Weathering of apatite released phosphate as well as REEs. Although calcite and dolomite generally contain substantially lower REE concentrations than apatite, their higher modal abundance may make them a substantial REE host phase (Chebotarev et al. 2022; Verplanck et al. 2022).

The formation of secondary REE phosphate minerals is a major control on REE enrichment in the laterite, and these phases are the focus of REE processing at the deposit. Investigation of other REE sequestration processes, including adsorption by other secondary phases, will help identify if other processes play important roles in REE enrichment.

5 Conclusions

The Mount Weld deposit is an example of economically viable REE deposit formed by lateritic weathering of a carbonatite. For an economically viable deposit, there must be sufficient in grade and tonnage as well have a mineralogy that enables economic mining and processing. The REE concentrations and size of the underlying carbonatite provided an adequate endowment of REEs for the laterite. Apatite in the carbonatite provided sufficient phosphate during weathering to facilitate the formation of secondary REE minerals in the laterite. The successful mining of the Mount Weld deposit offers a framework for evaluation of other carbonatite-derived laterites as viable REE deposits.

Acknowledgements

References

Anders E, Ebihara M (1982) Solar-system abundances of the elements. Geochimica et Cosmochimica Acta 46:2363-2280

Chebotarev DA, Wohlgemuth-Ueberwasser C, Hou T (2022) Partitioning of REE between calcite and carbonatitic melt containing P, S, Si at 650–900 °C and 100 MPa. Scientific Reports 12

Graham S, Lambert D, Shee S (2004) The petrogenesis of carbonatite, melnoite and kimberlite from the Eastern Goldfields Province, Yilgarn Craton. Lithos 76:519–533

Le Maître RW, ed. (2002) Igneous Rocks: a Classification and Glossary of Terms. Cambridge University Press, Cambridge, U.K. 193 p

Lynas Rare Earths LTD, 2022, Annual Report. 116 p

Verplanck PL, Farmer GL, Kettler RM, Lowers HA, Johnson CA, Koenig AE, Blessington MJ (2022) Petrogenesis and Rare Earth Element Mineralization of the Elk Creek Carbonatite, Nebraska, USA. Ore Geology Reviews 146

Verplanck PL, Mariano AN, Mariano AN Jr (2016) Rare earth element ore geology of carbonatites. In: Verplanck PL, d Hitzman MW (eds) Society of Economic Geologists Reviews in Economic Geology, v. 18, pp 5–32

Zhukova IA, Stepanov AS, Jiang S-Y, Murphy D, Mavrogenes JA, Allen C, Chen W, Bottrill R (2021) Complex REE systematics of carbonatites and weathering products from uniquely rich Mount Weld REE deposit, Western Australia. Ore Geology Reviews 39